

1 **A new biogeochemical modelling framework (FLaMe-v1.0) for lake methane**
2 **emissions on the regional scale: Development and application to the European**
3 **domain**

4 Manon Maisonnier¹, Maoyuan Feng^{1*}, David Bastviken², Sandra Arndt¹, Ronny Lauerwald³, Aidin
5 Jabbari⁴, Goulven Gildas Laruelle¹, Murray D. MacKay⁵, Zeli Tan⁶, Wim Thiery⁷, Pierre Regnier¹

6 ¹Biogeochemistry and Modelling of the Earth System-BGEOSYS, Department of Geoscience,
7 Environment and Society, Université Libre de Bruxelles, Brussels, Belgium

8 ²Linköping University, Department of Thematic Studies, Tema Environmental Change, Sweden

9 ³Université Paris-Saclay, INRAE, AgroParisTech, UMR Ecosys, Palaiseau, France

10 ⁴Environmental Fluid Dynamics Laboratory, Department of Civil Engineering, Queen's University,
11 Kingston, ON, Canada

12 ⁵Science and Technology Branch, Environment and Climate Change Canada, Toronto, M3H5T4,
13 Canada

14 ⁶Pacific Northwest National Laboratory, Richland, WA, USA

15 ⁷Department of Water and Climate, Vrije Universiteit Brussel, Brussels, Belgium

16

17 *Correspondence to Maoyuan Feng (maoyuan.feng@ulb.be)

Abstract

This study presents a new physical-biogeochemical modelling framework for simulating lake methane (CH₄) emissions at regional scales. The new model, FLaMe-v1.0 (Fluxes of Lake Methane), rests on an innovative, computationally efficient lake clustering approach that enables the simulation of CH₄ emissions across a large number of lakes. Building on the Canadian Small Lake Model (CSLM) that simulates the lake physics, we develop a suite of biogeochemical modules to simulate transient dynamics of organic Carbon (C), Oxygen (O₂), and CH₄-cycling. We first test the performance of FLaMe-v1.0 by analyzing physical and biogeochemical processes in two theoretical lakes with characteristics that can be considered representative for many lakes (an oligotrophic, deep lake driven by cold climate *versus* a ~~trophi~~e~~eutrophic~~, shallow lake driven by warm climate). Next, we evaluate the model by comparing simulated and observed timeseries of CH₄ emissions in four well-surveyed lakes. We then apply FLaMe-v1.0 at the European scale to evaluate simulated diffusive and ebullitive lake CH₄ fluxes against *in-situ* measurements in both boreal and central European regions. Finally, we provide a first assessment of the spatio-temporal variability in CH₄ emissions from European lakes ~~smaller than with a surface area comprised between 0.1–1000 km²~~ (n=108407, total area = 1.33x10⁵ km²), indicating a total emission of 0.97±0.23 Tg CH₄ yr⁻¹, with the uncertainty constrained by combining FLaMe-v1.0 and machine learning techniques. Moreover, 30% and 70% of these CH₄ emissions are through diffusive and ebullitive pathways, respectively. Annually averaged CH₄ emission rates per unit lake area during 2010–2016 have a South-to-North decreasing gradient, resulting in a mean over the European domain as 7.39 g CH₄ m⁻² yr⁻¹. Our simulations reveal a strong seasonality (with ice-blocking effects accounted for) in European lake CH₄ emissions, with ~~late summer emissions~~-nearly ten times higher emissions during late summer than during winter values. This pronounced seasonal variation highlights the importance of accounting for the sub-annual variability in CH₄ emissions to accurately constrain regional CH₄ budgets. In the future, FLaMe-v1.0

42 could be embedded into Earth System Models to investigate the feedback between climate warming
43 and global lake CH₄ emissions.

44 1. Introduction

45 Methane (CH₄) is the second most important greenhouse gas after carbon dioxide (CO₂), with a
46 Global Warming Potential (GWP) per mass ~28 times higher than that of CO₂ over a 100-year horizon
47 (Saunois *et al.*, 2020). Over the last centuries, the atmospheric CH₄ concentration has increased from
48 722 ppb in the pre-industrial period (year 1750) to 1923 ppb in year 2023 (Saunois, et al., 2020;
49 Dlugokencky, 2022; Forster *et al.*, 2024) and this increase is expected to continue in the future. The
50 critical role of CH₄ in global warming has called for the establishment of a comprehensive global
51 CH₄ budget, which embraces both natural and anthropogenic sources (Saunois *et al.*, 2016; 2020;
52 2024). This budget identified inland ~~waters (wetlands, freshwaters~~ (lakes, reservoirs, ponds, rivers,
53 etc.) as an important, yet highly uncertain atmospheric CH₄ source (Jackson *et al.*, 2020, 2024;
54 Saunois, *et al.*, 2020, Canadell *et al.*, 2021). Global lake CH₄ emissions, which has been estimated to
55 account for ~5 to 20% of total CH₄ emissions (576 TgCH₄ yr⁻¹), are the largest contributors to this
56 inland water source (Jackson *et al.*, 2020; Saunois *et al.*, 2020). However, estimates of its magnitude
57 vary depending on the assessment methods, with discrepancies of up to a factor of four (Saunois *et*
58 *al.*, 2020; DelSontro and John 2018; Rosentreter *et al.*, 2021; Bastviken *et al.*, 2011; Deemer *et al.*,
59 2016; Johnson *et al.*, 2021; Holgerson and Raymond 2016; Stavert *et al.* 2022). This variability in
60 global estimates also manifests itself at the continental scale. For instance, estimates of European lake
61 methane emissions range from 0.9 to 2.5 Tg CH₄ yr⁻¹ (Petrescu *et al.* 2021, 2023; Lauerwald *et al.*,
62 2023).

63 Observation-based upscaling approaches are highly dependent on the availability and quality of
64 *in-situ* measurements, which are unevenly distributed across the globe and biased towards summer
65 months (Canadell *et al.*, 2021; Johnson *et al.*, 2022). Although the number of CH₄ emission

66 measurements from lakes has increased considerably in recent decades, the two largest current
67 databases together contain only 1081 records from 575 lakes worldwide (Rosentreter *et al.*, 2021;
68 Johnson *et al.*, 2022). This relatively small data compilation is unlikely to capture the full diversity
69 of physical and biogeochemical patterns of >1.4 million lakes worldwide, which vary by morphology,
70 climate, trophic status, and underlying sediment characteristics (Rinta *et al.*, 2017; Bastviken 2004,
71 2022; Deemer and Holgerson 2021; Johnson *et al.*, 2022). Even more critically, the underlying data
72 collection was not designed to capture the inter-annual and decadal variability in CH₄ emissions
73 driven by climate change and nutrient dynamics, hence rendering the decomposition of the total lake
74 CH₄ fluxes into natural and human-induced components challenging (Saunois *et al.*, 2020). Finally,
75 although current instruments and techniques can effectively capture CH₄ fluxes through diffusive
76 (driven by gradients of aqueous CH₄ concentrations) and ebullitive (via gas bubbles in the sediments
77 due to oversaturation) emission pathways, measurements related to lake turnover events (release of
78 previously accumulated CH₄ due to stratification and ice cover) [and transport through vegetation](#)
79 [aerenchyma](#) remain highly challenging (Denfeld *et al.*, 2018; Mayr *et al.*, 2020; Zimmermann *et al.*,
80 2019). These limitations induce large uncertainties in observation-based upscaling methods. In this
81 context, process-based modelling approaches – that rely on detailed representations of lake physical
82 and biogeochemical processes informed and tested with the available observational data – offer
83 complementary strategies to help reduce these uncertainties.

84 Process-based biogeochemical models provide powerful tools to upscale scarce observations,
85 both in space and in time. In combination with the available observational datasets, they can help
86 deliver regional and global estimates of lake CH₄ emissions from daily to decadal timescales, as well
87 as future projections. These mechanistic models can also help identify the drivers such as climate,

land-use and atmospheric composition changes responsible for the complex temporal dynamics of lake CH₄ emissions. Over the last decades, several process-based models have thus emerged, e.g., LAKE 2.0 (Stepanenko *et al.* 2016), bLake4Me (Tan *et al.*, 2015), and ALBM (Tan *et al.*, 2018; 2024), to estimate lake CH₄ emissions to the atmosphere. These models explicitly account for the physical and biogeochemical processes that govern lake CH₄ dynamics and resulting emissions. For instance, using ALBM, Zhuang *et al.* (2023) recently estimated that global lakes (larger than 0.1 km²) emit 24.0 ± 8.4 Tg CH₄ yr⁻¹, which is at the lower end of the range reported by Saunio *et al.* (2020) and represents 11% of total global CH₄ emissions from natural sources as estimated from atmospheric inversions. Yet, these process-based models also have limitations that need to be addressed. A central limitation is the omission of lake phytoplankton productivity, which is one of the most reactive organic C sources and thus substrates for CH₄ production. In most of existing models, this key process and the associated microbial degradation of organic C is not simulated explicitly but taken as prescribed model inputs. If phytoplankton productivity and associated contributions of methane substrates can be incorporated in lake CH₄ models, this would allow capturing the impacts of environmental conditions beyond the commonly included direct temperature effects on organic matter decomposition and CH₄ production. Such additional important impacts include feedback of C metabolism on lake oxygen (O₂) cycling along with eutrophication effects on CH₄ emissions (Del Sontro *et al.*, 2018; Rosentreter *et al.*, 2021; Staver *et al.*, 2022). However, ~~including an explicit description of these processes it~~ is challenging, ~~because it requires to account for a~~ explicitly describe ~~the~~ suite of key physical and biogeochemical processes controlling the coupled C-O₂-CH₄ cycles while at the same time maintaining model complexity, as well as the needs for observational data and computational costs for regional and global scale applications with tractable bounds. In addition, it

110 also requires the quantification of nutrient inputs from the surrounding catchments, which exert a key
111 control on lake productivity.

112 To tackle ~~with~~ these challenges, we here develop a new process-based model framework of
113 intermediate complexity, FLaMe-v1.0 (Fluxes of Lake Methane version 1.0, ~~hereafter referred as~~
114 ~~FLaMe~~), that couples the C-O₂-CH₄ cycles in lakes using a one-dimensional representation.
115 Specifically, FLaMe-v1.0 builds upon the existing physical lake model CSLM (Canadian Small Lake
116 Model–MacKay, 2012; MacKay *et al.*, 2017), and extends with a novel biogeochemical module that
117 captures the production, oxidation, storage, transport and emissions of CH₄ in/from lakes. Importantly,
118 FLaMe-v1.0 introduces lake primary production and turnover of autochthonous organic carbon as a
119 major driver of lake O₂ and CH₄ dynamics. The coupled, mechanistic lake model is then embedded
120 in a computationally efficient clustering approach that allows for the application of the new, coupled,
121 mechanistic lake model for (i) large parameter/input ensemble runs on regional/global scales for
122 uncertainty assessments, (ii) long-term model projections for the assessment of future climate change
123 and its feedback on the Earth system, (iii) a potential coupling to Earth System Models (ESMs) in
124 subsequent stages of its development.

125 The structure of this paper is described as follows. In section 2, we provide a general description
126 of the lake model with a focus on a detailed description of the novel biogeochemical modules, as well
127 as the parameter choices and numerical solutions. In section 3, we first test the overall behavior of
128 FLaMe-v1.0 using two representative lakes (an oligotrophic, deep lake driven by cold climate *versus*
129 a trophic, shallow lake driven by warm climate), and then evaluate the simulated temporal variations
130 of CH₄ fluxes against observational data at four well-surveyed lakes in the real world. Next, we apply

FLaMe-v1.0 at the European scale and evaluate the results against *in-situ* measurements in boreal and central European lakes compiled by Rinta *et al.* (2017). Finally, we provide a spatio-temporally resolved estimate of CH₄ emissions from European lakes (2010–2016), assess their sensitivity to key model parameters, and constrain their uncertainty range using a machine-learning approach. In section 4, we discuss model limitations and potential directions for further research. Main conclusions and outlooks are drawn in section 5.

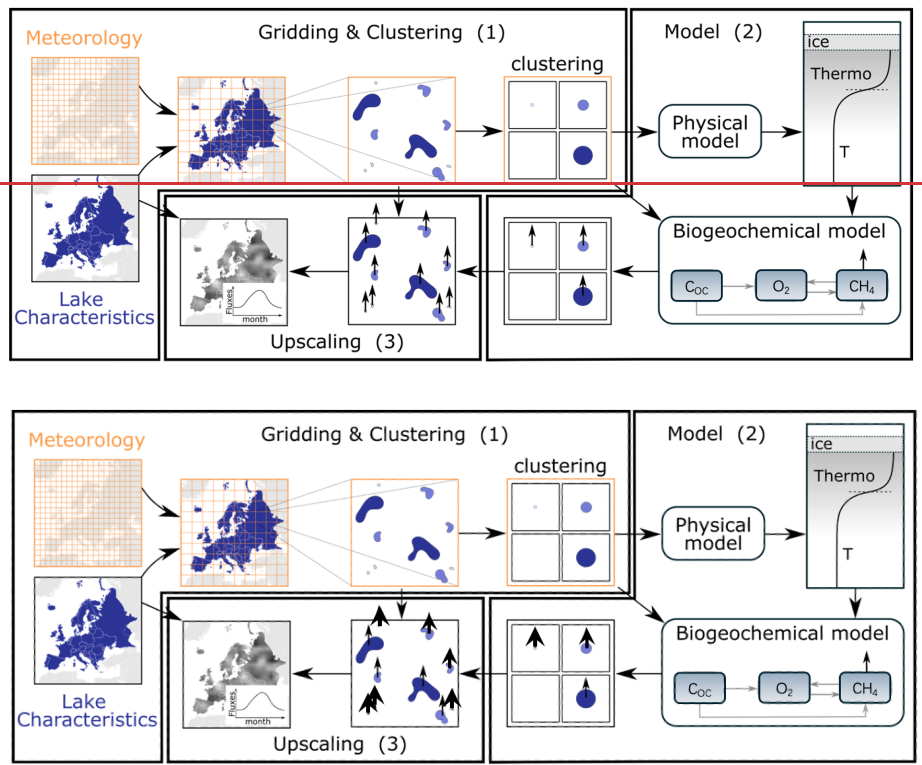
2. Methodology

2.1 General model approach

We developed a new process-based physical-biogeochemical model, FLaMe-v1.0 (Fluxes of Lake Methane), to simulate lake CH₄ production and emission at large spatial scales. FLaMe-v1.0 resolves the interplay of physical and biogeochemical processes that governs organic matter ($C_{OC,auto}$), oxygen (O₂), and methane (CH₄) dynamics to estimate (diffusive and ebullitive) lake CH₄ emissions, as well as CH₄ storage fluxes due to lake turnover and ice melting. To enable a continental-scale application of FLaMe-v1.0 (e.g., in Europe, $n=108407$ and total area = 1.33×10^5 km² for lakes with $0.1 \leq A_0 \leq 1000$ km² according to Messenger *et al.*, 2016; A_0 is the lake surface area), we here propose a lake clustering strategy to reduce the computational and data/input costs (Fig. 1) while resolving the variability in lake sizes, morphology, and trophic status as well as climate conditions across Europe. Within each grid cell ($2.5^\circ \times 2.5^\circ$), lakes are binned into four classes *arbitrarily* according to surface area (0.1–1 km², 1–10 km², 10–100 km², 100–1000 km²). We then run a FLaMe-set-up-v1.0 simulation for one representative lake per size class within each grid cell, using the arithmetic means of lake area, depth and trophic status of all lakes pertaining to the respective size class across the respective grid cell. Note that the areas and depths of all lakes are available from HydroLAKES

153 database (Messenger *et al.*, 2016) while trophic status is derived from outputs of the GlobalNEWS
 154 model (Mayorga *et al.*, 2010; Lauerwald *et al.*, 2019). The total emission flux from a given size class
 155 can be obtained by multiplying the CH₄ emission rates simulated by FLaMe-v1.0 with the total lake
 156 area of this size class (Fig. 1).

157



158

159 **Fig. 1. Illustration of the lake clustering and upscaling strategy for the continental application of FLaMe-v1.0**
 160 (Europe as an example). (1) Gridding and clustering: The European domain was divided into grid cells at a coarse
 161 spatial resolution of 2.5°×2.5°. Within each grid cell, lakes are clustered into four classes according to their surface
 162 areas. (2) FLaMe-v1.0 parallelization: FLaMe-v1.0 simulates the lake metabolic dynamics, vertically resolved

163 concentration and rate profiles of the coupled O₂-CH₄ cycle as well as diffusive and ebullitive CH₄ fluxes through
164 the water-air interface. The model was parallelized under transient conditions for each grid cell and each lake
165 class. (3) Upscaling: The areal rates (i.e., fluxes per unit lake surface area) simulated by FLaMe-v1.0 were then
166 multiplied by the total surface area of each lake class within each grid cell (available from HydroLAKES) and
167 aggregated at the monthly timescale. The arrows pertaining to clustered and original lakes represent the CH₄
168 emissions, and the arrow size represent the magnitude of the flux (i.e., a lower flux for larger lakes).

169 2.2 Model description

170 FLaMe-v1.0 builds on an online coupling approach between the Canadian Small Lake Model
171 (CSLM; MacKay, 2012; MacKay *et al.*, 2017) – a widely used lake physics model (Garnaud *et al.*,
172 2022; Versegghy and MacKay, 2017; William *et al.*, 2014) – and a set of newly developed
173 biogeochemical modules that resolve lake OC, O₂ and CH₄ dynamics. We selected the CSLM as the
174 basis of the representation of lake physical processes in FLaMe-v1.0 because CSLM was designed
175 for small lakes that accounts for >90 % of lakes (by number, mean depth <7.8 m) but contribute
176 disproportionally to lake CH₄ emissions in the European domain (HydroLAKES; Messenger *et al.*,
177 2016), as well as due to the expertise in our research team. CSLM simulates the following physical
178 variables: ~~of~~ temperature profile (T), thermocline depth (h_{mix} , at which the vertical temperature
179 gradient reaches its maximum), photic depth (h_{phot} , down to which the sunlight can penetrate, with
180 radiation density of at least 1% of that at the lake surface), and ice cover, which will be used to force
181 the biogeochemical modules (Fig. 2). In turn, the biogeochemical module will later modify the photic
182 depth simulated by CSLM to account for the effect of phytoplankton growth and self-shading on light
183 penetration, thus resolving the feedback between lake biogeochemical processes and lake physical
184 dynamics, hence forming a complete feedback loop. A detailed description of the well-established

CSLM model can be found in MacKay (2012) and MacKay *et al.* (2017) and is also briefly presented in Supplementary Text S1. Compared with other lake models (Table S1), the most important improvements in FLaMe-v1.0 are the adoption of a “valley” shape lake set up and the incorporation of autochthonous carbon dynamics (i.e., explicit simulation of primary production, decomposition, and oxygen processes) and its phosphorus limitation, which have been shown to be key control factors of CH₄ dynamics (Søndergaard *et al.*, 2017; Guildford and Heckay, 2000; Schindler, 1977). In what follows, we provide a detailed description of the vertically resolved 1D model set-up (section 2.2.1) used here, as well as of the novel biogeochemical modules (section 2.2.2 ~~and Table 1 for selected model parameter values~~). All the involved model parameters, their values, and ranges are summarized in Table 1 (section 2.3).

2.2.1 Model Scope: Idealized representation of lake morphology

Figure 2 illustrates the vertically resolved, one-dimensional model set-up of FLaMe-v1.0 that is used for both the physical and biogeochemical modules. The original version of CSLM usually adopts a “bucket” shaped morphology which assumes a constant area (A) versus water depth (z), i.e., $A(z) = A_0$, where A_0 is the lake surface area at $z = 0$ m. However, this morphology is unsuitable for the simulation of biogeochemical processes, especially when ~~the~~ variations in water depth within each lake are important. Therefore, we, instead, adopted a “valley” shaped lake morphology, with lake area $A(z)$ given by:

$$A(z) = \frac{A_0}{2s} (s + \operatorname{arctanh}(1 - 2(z/h_{\max})) \tanh(s)) \quad (1)$$

where A is the lake area (m²), z is the water depth (m), s is a shape parameter that controls the slope of the lakebed (a larger s indicates a steeper slope), and h_{\max} is the maximum lake depth. To ensure

206 that the volume (and hence heat exchange) is conserved between the “bucket” and “valley” shape set-
207 ups, the maximum depth of the valley-shape lake, h_{\max} , must be twice that of the mean depth of the
208 bucket-shape lake, h_{mean} (i.e., $h_{\max} = 2h_{\text{mean}}$), which was extracted from the global HydroLAKES
209 database compiled by Messenger *et al.* (2016). The bottom temperature profiles simulated by CSLM
210 were then extended to the maximal depth of the valley shape lake.

211 Physical processes in the water column are simulated by CSLM, on a one-dimensional, vertically
212 resolved, evenly distributed grid with a grid spacing of 50 cm. Each ~~layer of the water layer~~column
213 is connected to a vertically integrated lake sediment column of 5 m depth (h_s , m) ([Langenegger *et al.*, 2019](#)),
214 (Fig. 2). Since the CH₄ production rate decreases exponentially with sediment depth, ~~(not~~
215 ~~applicable to thermokarst lakes)~~, it is typically negligible at 5 m within the sediment column,
216 ([Langenegger *et al.*, 2019](#)), thus ensuring that the total, depth-integrated benthic CH₄ production
217 becomes insensitive to this arbitrary choice ~~(Langenegger *et al.*, 2019)~~. The surface area of each
218 sediment column in contact with the water column is determined by difference in the widths of two
219 adjacent water layers $A(z)$ (Eq. (1)). In addition, it should be noted that we assume no **horizontal**
220 material exchanges (O₂ and CH₄) between the sediments and water columns (i.e., across the interface
221 where left and right edges of a water layer touch the sediment box; Fig. 2), ~~while~~because of its
222 relatively minor magnitude compared to the vertical exchanges (Stepanenko *et al.*, 2016; Tan *et al.*,
223 2024) as well as the lack of observational data. Therefore, only the vertical exchanges are simulated
224 in this first version of the model (see details in the following sections).

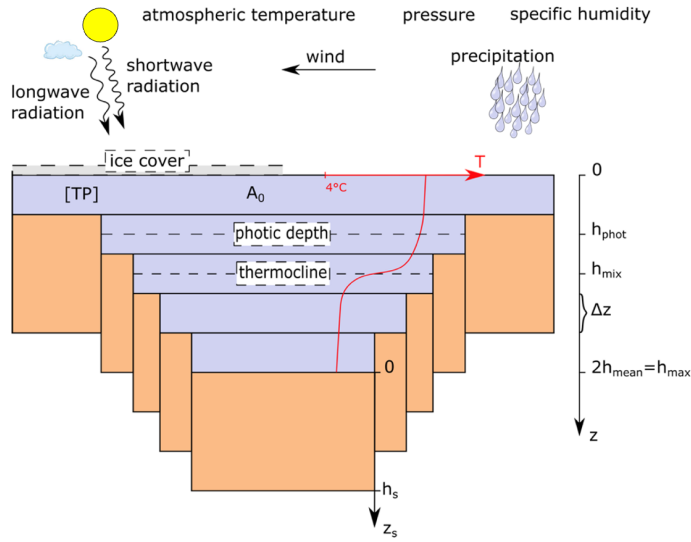


Fig. 2. Schematic representation of the lake morphology in FLAME-v1.0. The lake is represented by a “valley” shape (denoted by Eq. (1)). A_0 denotes the lake surface area, A is the area of each water layer, and h_{max} is the maximal water column depth. z represents the depth of a water column down to the surface of a sediment column while z_s stands for the depth inside a sediment column ($z_s = 0$ at the sediment water interface). The physical model is forced by longwave and shortwave radiation, near-surface wind, precipitation, atmospheric temperature, pressure, and specific humidity. Purple color indicates the water layers, and orange color indicates the sediment columns.

2.2.2 Biogeochemical Modules

2.2.2.1 Organic carbon module

Following the approach of Maavara *et al.* (2017), FLAME-v1.0 does not resolve the vertical distribution of labile (i.e., microbial degradable) organic carbon (OC) concentrations ($[C_{OC,auto}]$) produced by in-lake primary production, but only simulates the temporal dynamics of the volume-

238 integrated autochthonous OC stock ($\overline{C_{OC,auto}}$, g C) (the overbar here indicates a volume-integrated
 239 value). $\overline{C_{OC,auto}}$ should be understood as a simple indicator or an overall reflection of the resulting
 240 lake trophic status, itself controlled by the combined effects of climate and nutrient loads from the
 241 catchment. The allochthonous C inputs delivered from surrounding catchments are more refractory
 242 and ~~thus perform as less important substrates for CH₄ production (generally have a slower~~
 243 ~~decomposition rate (Grasset *et al.*, 2018; Guillemette *et al.*, 2017; DelSontro *et al.*, 2018-2018),~~
 244 ~~although CH₄ production from allochthonous OC has in some instances been reported to be higher~~
 245 ~~than from autochthonous compounds in laboratory incubations (Grasset *et al.*, 2018).~~ Thus, ~~we~~
 246 ~~consider the allochthonous OC as less important substrates for CH₄ production, and consider the~~
 247 ~~autochthonous primary production is considered as the only labile OC source, neglecting in this first~~
 248 ~~model version; the allochthonous OC contribution in this first version will be added in the future~~
 249 ~~upgrade of FLaMe the model.~~

250 The temporal evolution of volume-integrated labile OC stock is determined by the interplay
 251 between autochthonous primary production, pelagic and benthic mineralization and burial fluxes
 252 (Maavara *et al.*, 2017):

$$253 \quad \frac{\partial \overline{C_{OC,auto}}}{\partial t} = \overline{F_{PP}} - \overline{F_{Min}} - \overline{F_{Bur}} \quad (2)$$

254 where t is time (day), and $\overline{C_{OC,auto}}$ is the volume-integrated OC stock (g C). $\overline{F_{PP}}$, $\overline{F_{Min}}$ and $\overline{F_{Bur}}$ are
 255 the volume-integrated primary production, mineralization, and sedimentary burial fluxes (g C d⁻¹),
 256 respectively. Following Maavara *et al.* (2017), we assume that autochthonous primary production
 257 rates are controlled by the light regime, water temperature, and the lake total dissolved phosphorus

258 ($\overline{F_{PP}}$) concentration ($\overline{F_{PP}}$, g P m⁻³) (Reynolds, 2006). The volume-integrated $\overline{F_{PP}}$ can then
 259 be expressed using a classical Michaelis-Menten formulation (Mavaara *et al.*, 2017):

$$260 \quad \overline{F_{PP}} = B P_{Chl,max} M(T_{mean}) \frac{[TP]}{K_{s,P} + [TP]} \frac{[TP]}{K_{s,P} + [TP]} V_{phot} \quad (3)$$

261 where B is the phytoplankton biomass (expressed as chlorophyll-a concentration, g Chl-a m⁻³) in the
 262 photic zone (Eq. (5)), $P_{Chl,max}$ is the maximum carbon fixation rate per unit of chlorophyll-a (g C (g
 263 Chl-a)⁻¹ h⁻¹), M is a dimensionless metabolic correction factor that depends on the mean lake water
 264 temperature in photic zone T_{mean} (°C) (see Eq. (4)), $K_{s,P}$ is the half-saturation constant for phosphorus
 265 limitation (g P m⁻³), and V_{phot} is the water volume above the photic depth (m³). Parameters $P_{Chl,max}$
 266 and $K_{s,P}$ are constrained based on published observations (see section 2.3), while the metabolic factor
 267 M is given by:

$$268 \quad M(T_{mean}) = \begin{cases} 1, & T_{mean} \geq 28^\circ\text{C} \\ Q_{10,prod}^{\frac{T_{mean}-28}{10}}, & T_{mean} < 28^\circ\text{C} \end{cases} \quad (4)$$

269 where $Q_{10,prod}$ is the temperature sensitivity for primary production, quantifying the increases of the
 270 metabolic factor per 10 degree increase in temperature. Surface water phytoplankton biomass, B , is
 271 approximated by a function of the photosynthetically active radiation (PAR), which is determined
 272 by shortwave radiation and light extinction in the water column:

$$273 \quad B = \left(\frac{1}{k_c}\right) (0.75 \left(\frac{PP}{RP}\right) \ln \left(\frac{0.7 PAR_0}{0.5 PAR_k}\right) \left(\frac{1}{h_{prod}}\right) - (K_{dw} + K_{dp} + K_{dg})) \quad (5)$$

274 where k_c is the absorbance of PAR per unit of chlorophyll-a (m² (g Chl-a)⁻¹), and PP/RP is the ratio
 275 of maximum gross photosynthesis to respiration per unit chlorophyll-a. PAR_0 is the PAR at the lake
 276 surface (μmol m⁻² s⁻¹), determined by the incoming shortwave radiation, as well as the daytime that
 277 is specified by lake latitude and phenology (represented by the day of the year). PAR_k is the PAR at

the onset of photosaturation ($\mu\text{mol m}^{-2} \text{s}^{-1}$). The productive depth h_{prod} is determined as the maximum of the thermocline and the photic depth simulated by the physical model. K_{dw} , K_{dp} , and K_{dg} represent nonalgal *PAR* attenuations, due to pure water, inorganic suspended particulate matter, and labile carbon, respectively. Following Lewis (2011), K_{dg} is calculated as a function of $[C_{OC,auto}]$ as:

$$\ln(K_{dg}) = -4.44 + 1.80\ln([C_{OC,auto}]) - 0.149(\ln([C_{OC,auto}]))^2. \quad (6)$$

Eq. (5) was derived based on the assumption of a balance between production and respiration (Reynolds, 2006; Lewis, 2011). Here we slightly relax this assumption and assume near-equilibrium conditions for given climate conditions at the monthly timescale, allowing us to simulate seasonal variations of primary production and associated biogeochemical processes. Note that this assumption is only used for biogeochemical variables related to primary production, while physical variables simulated by CSLM are resolved at a sub-daily time step.

Following Hanson *et al.* (2011; 2014) and Maavara *et al.* (2019), the volume-integrated mineralization rate is simulated as a function of temperature and labile OC availability:

$$\overline{F_{Min}} = k_{20} \theta^{T_{mean}-20} \overline{C_{OC,auto}} \quad (7)$$

where k_{20} is a first-order rate constant for the mineralization of $\overline{C_{labile}}$ at 20 °C (d^{-1}). T_{mean} is the mean water temperature (°C) in photic zone, and θ is the temperature dependence of mineralization of organic matter (Hanson *et al.*, 2014).

Following Maavara *et al.* (2019), the burial flux $\overline{F_{Bur}}$ is represented by a first order process driven by the labile OC stock $\overline{C_{OC,auto}}$:

$$\overline{F_{Bur}} = k_{bur} \overline{C_{OC,auto}} \quad (8)$$

where k_{bur} is the burial rate constant and here set as half of the mineralization rate constant following the ratios between these two processes reported in the global lake dataset ($n=230$) assembled by Mendonça *et al.* (2017). This ratio is likely an upper bound because it accounts for contributions of both autochthonous and allochthonous carbon sources in the dataset, while allochthonous inputs should have ~~distinct (but unquantified)~~ higher burial/decomposition ratios ~~from than~~ autochthonous ones (Mendonça *et al.*, 2017; Guillemette *et al.*, 2017).

2.2.2.2 Methane module

The methane module simulates the dynamics of CH_4 concentration in both sediment and water columns as controlled by ~~benthic~~ CH_4 production, aerobic CH_4 oxidation, and diffusive and ebullitive transport from sediment to water and atmosphere (Fig. 3). Since the observational evidence suggests that benthic CH_4 production is the dominant CH_4 source in lakes (Tan *et al.*, 2015; Bastviken, 2022), we neglect the CH_4 production within the lake's water column in the model.

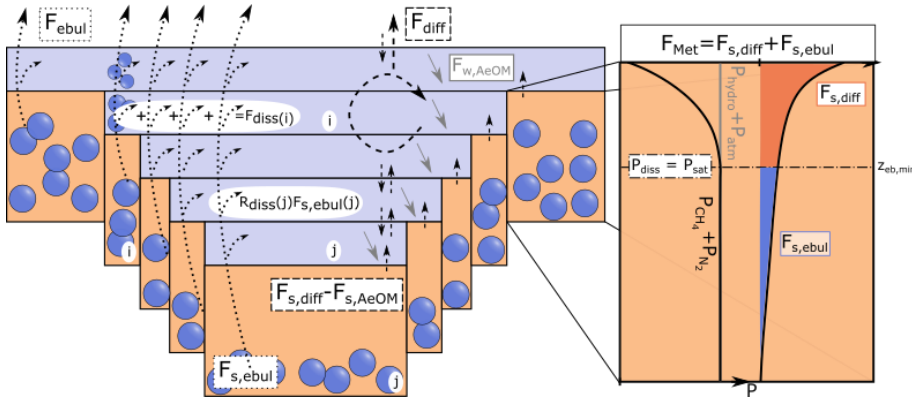


Fig. 3. Illustration of the methane (CH₄) module of FLAME with a zoom into benthic CH₄ dynamics (zoom modified from Langenegger *et al.*, 2019). Benthic CH₄ production (zoom) assumes an exponential decrease in CH₄

314 production rate (F_{Met}) with depth. The CH_4 and N_2 partial pressures ($P_{CH_4} + P_{N_2}$) is mainly driven by the CH_4
 315 production and follows the black curve profile, which starts to exceed the sum of the hydrostatic and atmospheric
 316 pressure ($P_{hydro} + P_{atm} - P_{H_2O}$, grey line) at $z_{eb,min}$. Thus, this depth ($z_{eb,min}$) divides F_{Met} into a diffusive ($F_{s,diff}$, red
 317 filled region) and an ebullitive ($F_{s,ebul}$, cyan filled region) flux. $F_{s,AeOM}$ and $F_{w,AeOM}$ are the CH_4 oxidation in the
 318 sediment and water column, respectively. F_{diss} is the dissolution of the gas bubbles during transport through the
 319 water column. F_{diff} and F_{ebul} are diffusive and ebullitive CH_4 fluxes through the water-air interface, respectively. i
 320 and j are the indexes of water layers and sediment columns. Note that the sediment column pertaining to a
 321 particular water layer has the same index as that water layer.

322 Within the lake sediment, CH_4 dynamics are determined by the balance between CH_4 production
 323 via methanogenesis and CH_4 migration to the water column through diffusive and ebullitive
 324 transport:

$$325 \quad \frac{\partial CH_{4,s}(z)}{\partial t} = \widetilde{F_{Met}}(z) - \widetilde{F_{s,diff}}(z) - \widetilde{F_{s,ebul}}(z) \quad (9)$$

$$326 \quad \widetilde{F_{Met}}(z) = f_{mm} \frac{M_{CH_4}}{M_C} \overline{F_{Min}} \frac{V_s(z)}{V_{s,tot}} \quad (10)$$

327 where the tilde overbar here represents the volume-integrated stocks or fluxes in the sediment
 328 column, which is different from the straight overbar for volume-integrated values in the water
 329 column. Note that we have sediment columns at different water depths, such that the stocks and
 330 fluxes are represented as a function of water depth z , which is characterized by the valley-shape
 331 model set-up and different from the conventional bucket shape set-up. $CH_{4,s}(z)$ is thus the volume-
 332 integrated CH_4 stock for the sediment column with the sediment-water interface positioned at depth
 333 z (g CH_4). $\widetilde{F_{Met}}(z)$ is the volume-integrated flux of CH_4 production through the entire sediment
 334 column with a sediment-water interface at depth z (g CH_4 d⁻¹), and $\widetilde{F_{s,diff}}(z)$ and $\widetilde{F_{s,ebul}}(z)$ are

335 volume-integrated diffusive and ebullition fluxes ($\text{g CH}_4 \text{ d}^{-1}$) through the sediment-water interface
 336 at depth z , respectively. f_{mm} denotes the fraction of organic matter mineralization that proceeds via
 337 methanogenesis according to data compiled by Hanson *et al.* (2014) and Bastviken (2022). $M_{\text{CH}_4}/M_{\text{C}}$
 338 is a conversion factor corresponding to the molar ratio of CH_4 to COC_{auto} . As $f_{\text{mm}} \frac{M_{\text{CH}_4}}{M_{\text{C}}} \overline{F_{\text{Min}}}$ is the
 339 total CH_4 production flux integrated over the whole water column, we assume that the fractions of
 340 CH_4 production occurring in different sediment columns are set according to their volume
 341 proportions, i.e., $\frac{V_s(z)}{V_{s,\text{tot}}}$.

342 The partitioning of CH_4 production into ebullitive and diffusive fluxes depends on the porewater
 343 CH_4 concentration or its partial pressure, which relies mainly on the vertical distribution of CH_4
 344 production rate in the sediment as well as the oxygen concentration (but is of second-order
 345 importance). Based on the observation-based assumption that the organic carbon concentration and
 346 thus mineralization rates exponentially decrease with sediment depth, we here assume an
 347 exponentially decreasing relationship between methanogenesis rate versus depth (Fig. 3), following
 348 Langenegger *et al.* (2019):

$$349 \quad f_{\text{met}}(z, z_s) = F_{\text{Met},0}(z) \exp(-\alpha z_s) \quad (11)$$

350 where $f_{\text{met}}(z, z_s)$ is the methanogenesis rate ($\text{g CH}_4 \text{ m}^{-3} \text{ d}^{-1}$) at sediment depth z_s for the sediment
 351 column with the sediment-water interface positioned at depth z . $F_{\text{Met},0}(z)$ is the maximum CH_4
 352 production at the sediment-water interface ($\text{g CH}_4 \text{ m}^{-3} \text{ d}^{-1}$) at depth z , and α is a shape parameter
 353 (m^{-1}) that controls the decrease of methanogenesis rate with depth. As the shape of this curve
 354 typically depends on the flux of labile carbon settling on the lake bottom, and thus, lake trophic
 355 status, the parameter α is here scaled by the F_{PP} empirically:

$$\alpha = \alpha_{min} + \beta \cdot F_{PP} \frac{V_w}{V_{phot}} \quad (12)$$

where α_{min} is the minimum or base value, and β is the dependence of α on F_{PP} . The values of α_{min} and β are determined based on the measurements in lakes of different trophic status reported by Langenegger *et al.* (2019).

To determine the maximum CH₄ production $F_{Met,0}(z)$, the integral of CH₄ production rate over sediment column should equal to the volume-integrated CH₄ production flux $\overline{F_{Met}}(z)$ as specified by Eq. (10):

$$A_s(z) \int_0^{h_s} f_{met}(z, z_s) dz_s = \overline{F_{Met}}(z) \quad (13)$$

where $A_s(z)$ is the surface area of sediment column in contact with the water layer at lake depth z and is determined by difference in the areas of two adjacent water layers $A(z)$ (Eq. (1)). The maximum CH₄ production at depth z , $F_{Met,0}(z)$, can be obtained by combining Equations (10), (11) and (13):

$$F_{Met,0}(z) = \frac{\overline{F_{Met}}(z)}{A_s(z)} \frac{\alpha}{1 - \exp(-\alpha h_s)} \quad (14)$$

Since CH₄ production increases the *in-situ* CH₄ concentration as the sediment depth increases, the CH₄ concentration may exceed its solubility concentration and methane gas bubbles may start forming (Fig. 3). To constrain the partitioning of CH₄ production between diffusion and ebullition, the threshold sediment depth, $z_{eb,min}$, at which CH₄ concentration starts to exceed the solubility limit, is determined based on the equilibrium pressure condition following Langenegger *et al.* (2019) (see details in Supplementary Text S2). In the upper portion of the sediment column ($z_s < z_{eb,min}$), the

376 produced CH₄ will diffuse into water; however, a fraction of the diffusing CH₄ will be oxidized in
 377 the transit through the upper sediment column, and only the remaining CH₄ will reach the sediment-
 378 water interface. The volume-integrated CH₄ oxidation in the sediment at depth z , $\widetilde{F_{s,AeOM}}(z)$, is here
 379 assumed to be controlled by the O₂ concentration in the overlying bottom water, and is represented
 380 by a Michaelis-Menten function:

$$381 \quad \widetilde{F_{s,AeOM}}(z) = \widetilde{F_{Met}}(z) \frac{[O_2]_z}{K_{s,O_2} + [O_2]_z} \quad (15)$$

382 where K_{s,O_2} is the half-saturation constant of O₂ for the sedimentary CH₄ oxidation. As a result, the
 383 diffusive flux passing through the sediment-water interface is determined as follows:

$$384 \quad \widetilde{F_{s,diff}}(z) = A_s(z) \int_0^{z_{eb,min}} \widetilde{F_{Met,0}}(z) \exp(-\alpha z_s) dz_s - \widetilde{F_{s,AeOM}}(z) \quad (16)$$

385 In the lower portion of the sediment column ($z_s > z_{eb,min}$; where oversaturation occurs), the
 386 produced CH₄ feeds the ebullitive flux, with the volume-integrated value $\widetilde{F_{s,ebul}}(z)$ (g CH₄ d⁻¹) as
 387 given by:

$$388 \quad \widetilde{F_{s,ebul}}(z) = A_s(z) \int_{z_{eb,min}}^{h_s} \widetilde{F_{Met,0}}(z) \exp(-\alpha z_s) dz_s \quad (17)$$

389 Note that Equations. (16) and (17) implicitly imply that, at the monthly resolution of our model, the
 390 CH₄ dynamics in the sediment is at steady state and all the CH₄ produced during this time interval
 391 is either oxidized or released through the water column via diffusive and ebullitive pathways.

392

393 Pelagic, dissolved CH₄ diffuses in the water column and its concentration is determined by the
 394 diffusive CH₄ flux passing through the sediment-water interface (acting as a source for each water
 395 layer), by aerobic CH₄ oxidation in the water column, and by the re-dissolution of the ebullitive CH₄

396 fluxes during transit through the water column. The mass conservation equation of dissolved CH₄ is
 397 then given by:

$$398 \quad \frac{\partial[\text{CH}_4]_w}{\partial t} = \frac{\partial}{\partial z} \left(K_{diff} \frac{\partial[\text{CH}_4]_w}{\partial z} \right) + \widetilde{F_{s,diff}}(z) \frac{I}{A(z)dz} - F_{w,AeOM}(z) + F_{diss}(z) \quad (18)$$

399 where [CH₄]_w is the pelagic CH₄ concentration (g CH₄ m⁻³) and K_{diff} is the eddy diffusion coefficient
 400 of CH₄ in water (m² d⁻¹). $\widetilde{F_{s,diff}}(z) \frac{I}{A(z)dz}$ is the change of CH₄ concentration induced by diffusive
 401 inputs from the sediment columns, the term A(z)dz being the volume of the water layer connected
 402 to the corresponding sediment column. F_{w,AeOM}(z) is the aerobic CH₄ oxidation rate in the water
 403 column, and is described through double Michaelis-Menten reaction kinetics (Stepanenko *et al.*,
 404 2016; Liikanen *et al.*, 2002; Thottathil and Prairie, 2019):

$$405 \quad F_{w,AeOM}(z) = k_{max} Q_{10,ox}^{\frac{T-T_r}{10}} \frac{[\text{CH}_4]_{w,z}}{K_{s,\text{CH}_4} + [\text{CH}_4]_{w,z}} \frac{[\text{O}_2]_z}{K_{s,\text{O}_2} + [\text{O}_2]_z} \quad (19)$$

406 where k_{max} is the maximum CH₄ oxidation rate (Liikanen *et al.* 2002), T is the water temperature, T_r
 407 is the reference temperature, and Q_{10,ox} expresses the temperature dependency of the CH₄ oxidation
 408 rate. K_{s,CH₄} and K_{s,O₂} are the half-saturation constants for CH₄ and O₂, respectively.

409 To constrain the redissolution of gas bubbles (F_{diss}(z)), we follow the approach proposed by
 410 McGinnis *et al.* (2006) where a function (f_{bdiss}(z)) is used to represent the fraction of the benthic
 411 ebullitive CH₄ flux that redissolves in the water column during gas ascent. This fraction is a function
 412 of water depth and gas bubble diameter, and the latter was set to 5 mm following Delwiche and
 413 Hemond (2017). With this function f_{bdiss}(z), the redissolved CH₄ fluxes from sediment column at
 414 depth z are assumed to be evenly redistributed in the water layers above the sediment, i.e.,

$$415 \quad f_{rediss}(z) = \frac{f_{bdiss}(z) \widetilde{F_{s,ebul}}(z)}{\int_0^z A(z)dz} \quad (20)$$

416 where $\int_0^z A(z)dz$ is the water volume above the sediment layer at the depth of interest z . Then, at
 417 this particular depth z , the redissolution flux (F_{diss} , g CH₄ m⁻³ d⁻¹) is thus determined as follows:

$$418 \quad F_{diss}(z) = \int_z^{h_{max}} f_{rediss}(z)dz \quad (21)$$

419 where $\int_z^{h_{max}} f_{rediss}(z)dz$ represents the integral of all re-dissolved ebullitive fluxes from sediment
 420 columns below z .

421 By deducing this dissolution flux from the ebullitive flux released from lake sediments, the
 422 resultant ebullitive flux reaching the atmosphere (F_{ebul} ; g CH₄ m⁻² d⁻¹) is calculated as:

$$423 \quad F_{ebul} = \frac{1}{A_0} \int_0^{h_{max}} (1 - f_{bdiss}(z)) \widetilde{F_{s,ebul}}(z)dz \quad (22)$$

424 where A_0 is the lake surface area, and $(1 - f_{bdiss}(z)) \widetilde{F_{s,ebul}}(z)$ is the component of ebullitive flux at
 425 depth z that reaches the atmosphere.

426 In addition to diffusive and ebullitive pathways, FLAME-v1.0 also calculates a storage flux (F_{stor})
 427 that encapsulates the changes in the total CH₄ mass stored in hypolimnion due to the weakening of
 428 lake stratification or turnover events when the lake surface temperature ~~erosses~~approaches the
 429 ~~threshold of critical temperature~~ 4°C (MacKay, 2012; MacKay *et al.*, 2017). This results in a full
 430 mixing of the lake that releases the previously accumulated CH₄ in the anoxic portion of the lake
 431 and concomitantly fully aerates the water column. Lake turnovers thus lead to a complete
 432 homogenization of O₂ and CH₄ concentration across the vertically resolved water column. Before
 433 lake turnover, the lake water is highly stratified, blocking the material exchange between upper and
 434 lower water layers, such that bottom water has high CH₄ concentration (even oversaturated) and low
 435 O₂, while the upper water has high O₂ concentration and low CH₄ concentration. Upon full mixing,

remobilization of larger CH₄ stocks that accumulated in the hypolimnion abruptly increase the CH₄ concentration near the lake surface, and hence strongly enhance the diffusive flux through the air-water interface. ~~That is, the storage flux in FLAME; in the meantime, O₂ in the upper layers can penetrate to deep water layers and start oxidizing the CH₄ throughout the entire water column. After full mixing, the CH₄ emissions and oxidation are both simulated based on O₂ and CH₄ concentrations within each water layers. That is, the storage flux in FLAME-v1.0~~ is not simulated separately but it is implicitly incorporated into the diffusive flux F_{diff} which increases dramatically following the formation of a very sharp CH₄ concentration gradient at the lake surface.

2.2.2.3 Oxygen module

The oxygen module is needed to simulate the lake methane processes (section 2.2.2.2). It represents the O₂ cycle within the water column, driven by O₂ production by photosynthesis, O₂ consumption by pelagic and benthic OC mineralization, and aerobic pelagic and benthic CH₄ oxidation. These processes are coupled to the vertical diffusive transport of O₂ through water column (Fig. 4). The one-dimensional conservation equation for O₂ concentration in the water column is thus given by:

$$\frac{\partial [O_2]}{\partial t} = \frac{\partial}{\partial z} (K_{diff} \frac{\partial [O_2]}{\partial z}) + OF_{PP}(z) - OF_{w,Aer}(z) - \frac{I}{A(z)dz} OF_{s,Aer}(z) - OF_{w,AeOM}(z) - OF_{s,AeOM}(z) \quad (23)$$

where [O₂] is the O₂ concentration in the water (g O₂ m⁻³), and K_{diff} is the eddy diffusion coefficient of O₂ (m² d⁻¹), assumed identical to that of CH₄. $OF_{PP}(z)$ is the oxygen production through primary production (g O₂ m⁻³ d⁻¹) at depth z . $OF_{w,Aer}(z)$ is the O₂ consumption by heterotrophic respiration (g O₂ m⁻³ d⁻¹) in the water column at depth z , while $OF_{s,Aer}(z)$ is the volume-integrated O₂ consumption by heterotrophic respiration in the sediment (g O₂ m⁻³ d⁻¹), and $A(z)dz$ is the volume of the water layer connected to the corresponding sediment column. $OF_{w,AeOM}(z)$ and $OF_{s,AeOM}(z)$ are

the aerobic CH_4 oxidation in the water column and sediment ($\text{g O}_2 \text{ m}^{-3} \text{ d}^{-1}$), respectively, at depth z .

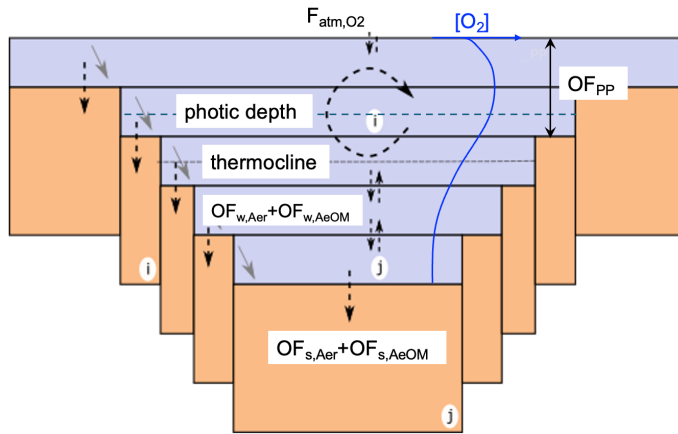


Fig. 4. Illustration of the oxygen (O_2) module in the FLAME-model-v1.0. The O_2 production due to primary production occurs only in the photic zone (OF_{PP}), while the O_2 consumption by heterotrophic respiration occurs in both the entire pelagic zone and benthic zone ($\text{OF}_{w,Aer}$ and $\text{OF}_{s,Aer}$). The O_2 consumption due to CH_4 oxidation occurs also in both pelagic and benthic zones ($\text{OF}_{w,AeOM}$ and $\text{OF}_{s,AeOM}$). In this figure, the dotted arrows crossing the sediment-water interface represent the O_2 demands in sediments ($\text{OF}_{s,Aer}$ and $\text{OF}_{s,AeOM}$), the dashed arrows represent the eddy diffusion of O_2 between water layers and through the water-air interface, and the tilted grey arrows represent the aerobic oxidation of CH_4 in the water column. As a result, the blue curve depicts a typical vertical profile of O_2 concentration under lake water stratification.

Photosynthesis occurs only in the photic zone, and the amount of O_2 produced by primary production $\overline{\text{OF}_{PP}}$ (volume-integrated value; $\text{g O}_2 \text{ d}^{-1}$) can be determined according to the stoichiometric ratio M_{O_2}/M_C , where M_{O_2} and M_C are the molar masses of oxygen and carbon,

472 respectively. To resolve the vertical O₂ profile, the O₂ produced during primary production is
 473 assumed to be evenly redistributed within the water layers above the photic depth (Fig. 4):

$$474 \quad OF_{PP}(z) = \begin{cases} \overline{F_{PP}} \frac{1}{V_{phot}} \frac{M_{O_2}}{M_C}, & z < z_{phot} \\ 0, & z \geq z_{phot} \end{cases} \quad (24)$$

475 where V_{phot} is the photic volume.

476 The oxygen consumption induced by CH₄ oxidation in the sediment and water column can be
 477 calculated from corresponding CH₄ fluxes (Eqs. (15) and (19), respectively) and the stoichiometry
 478 of the reactions involved:

$$479 \quad OF_{s,AeOM}(z) = \frac{2M_{O_2}}{M_{CH_4}} F_{s,AeOM}(z) \quad (25)$$

$$480 \quad OF_{w,AeOM}(z) = \frac{2M_{O_2}}{M_{CH_4}} F_{w,AeOM}(z) \quad (26)$$

481 As in Eq. (10), a fraction of the mineralized organic carbon (represented by f_{mm}) is channeled
 482 into the methanogenesis pathway according to the data compiled by Hanson *et al.* (2014) and
 483 Bastviken (2009). Thus, the remaining fraction ($1-f_{mm}$) of the total mineralization $\overline{F_{Min}}$ is channeled
 484 into the aerobic metabolic pathway (F_{Aer}). As a result, the *bulk volumetric rate* of oxygen
 485 consumption due to the aerobic metabolic activity (OF_{Aer}) can be represented by the fraction $1-f_{mm}$
 486 and the volume-integrated mineralization $\overline{F_{Min}}$:

$$487 \quad OF_{Aer} = (1-f_{mm}) \overline{F_{Min}} \frac{1}{V_w} \frac{M_{O_2}}{M_C} \quad (27)$$

488 In the sediment, the aerobic mineralization occurs only in the upper oxic layer. The thickness
 489 of this aerobic layer is limited by the oxygen penetration depth z_{ox} . Following Ruardij and Van

490 Raaphorst (1995), this depth z_{ox} can be derived by solving the steady-state reaction-diffusion
 491 equation for O_2 in the sediment:

$$492 \quad z_{ox} = \sqrt{\frac{2K_{s,diff}}{OF_{s,AeOM} + OF_{Aer}}} \quad (28)$$

493 where $K_{s,diff}$ is the molecular diffusion coefficient within the sediment, which is dependent on the
 494 temperature (Ruardij and Van Raaphorst, 1995). The amount of O_2 consumed within the oxic layers
 495 of the sediment can thus be determined as:

$$496 \quad \widetilde{OF_{s,Aer}}(z) = OF_{Aer} A_s(z) z_{ox} \quad (29)$$

497 where $A_s(z)$ is the area of the corresponding sediment column at depth z . To ensure a mass balance,
 498 the volumetric rate of O_2 consumption due to aerobic metabolism in water can then be calculated
 499 as follows:

$$500 \quad OF_{w,Aer}(z) = OF_{Aer} - \widetilde{OF_{s,Aer}}(z) \frac{1}{A(z)dz} \quad (30)$$

501 where $A(z)dz$ is the volume of the water layer connected to the corresponding sediment column, and
 502 it is used here to convert the sedimentary O_2 consumption into a volumetric rate in the water column.
 503 Furthermore, following Martin *et al.* (1987), Carlson *et al.* (1994) and Arístegui *et al.* (2003), we
 504 redistribute the respiration ($OF_{w,Aer}$) within the water column, assuming that 80% of the respiration
 505 occurs in the photic zone, with the remaining 20%, sustained by the export production, occurs in the
 506 deeper water layers where it can further degrade.

507 2.2.3 Boundary conditions for the transport module

508 The partial differential equations (18) and (23) require boundary conditions to constrain the
 509 diffusive transport (i.e., the first term on the right-hand side of both equations). At the sediment-

water interface, a zero-flux boundary condition is imposed, because the diffusive exchanges of CH₄ and O₂ between the sediment columns and the overlying waters are already included as source/sink terms in Eq. (18) and (23). This choice was guided by the valley-shape configuration of our lake set-up, and thus by the presence of diffusive CH₄ and O₂ exchange fluxes with sediment in each water layer of our model, a situation in stark contrast from a bucket shape model where only a single sediment column would be connected to the bottom water layer.

At the lake surface ($z = 0$ m), the boundary conditions are determined by the CH₄ and O₂ exchange fluxes with the atmosphere, as given by (Wanninkhof et al., 2009; Cole and Caraco, 1998):

$$F_{\text{atm,CH}_4} = k_{ge}([CH_4] - f_{CH_4,atm} P_{\text{atm}} M_{CH_4} K_{H,CH_4} \exp(\frac{\partial \ln(K_{H,CH_4})}{\partial T} (\frac{1}{T_l} - \frac{1}{298.15}))) \quad (31)$$

$$F_{\text{atm,O}_2} = k_{ge}([O_2] - f_{O_2,atm} P_{\text{atm}} M_{O_2} K_{H,O_2} \exp(\frac{\partial \ln(K_{H,O_2})}{\partial T} (\frac{1}{T_l} - \frac{1}{298.15}))) \quad (32)$$

where $F_{\text{atm,CH}_4}$ and $F_{\text{atm,O}_2}$ are diffusive fluxes of CH₄ (g CH₄ m⁻² d⁻¹) and O₂ (g O₂ m⁻² d⁻¹) through the air-water interface of the lake, respectively. $f_{CH_4,atm}$ and $f_{O_2,atm}$ are molar fractions of CH₄ and O₂ in the atmosphere, respectively, and P_{atm} is the atmospheric pressure. K_{H,CH_4} and K_{H,O_2} are Henry's constants of CH₄ and O₂ at 298.15 K and k_{ge} is the piston velocity (m s⁻¹), here constrained from the empirical equation reported by Cole and Caraco (1998), as in Tan *et al.* (2015; 2018) and Stepanenko *et al.* (2016):

$$k_{ge} = (C_{k1} + C_{k2} v_{a,10}^n) \sqrt{\frac{600}{S_{CX}}} \quad (33)$$

where C_{k1} , C_{k2} and n are empirical constants (Cole and Caraco, 1998). $v_{a,10}$ is the absolute wind velocity measured at 10 m above the lake surface (m s⁻¹), and S_{c,CH_4} and S_{c,O_2} are the Schmidt number of CH₄ and O₂, respectively (Wanninkhof *et al.* 2009). Note that more ~~recently~~ ~~new~~ recent

formulations of k_{ge} have been ~~proposed~~ (published in the last decade (Wanninkhof *et al.* 2014; McIntire *et al.*, 2020) but we here choose to use Eq. (33) ~~following~~to be consistent with previous lake modelling studies (Tan *et al.*, 2015; Stepanenko *et al.* 2016; Tan *et al.*, 2018).

2.3 Parameter values

Table 1 summarizes all physical and biogeochemical parameters, their values, as well as the original references from which they were extracted. Most of these parameters were either directly taken from relevant modelling studies or constrained based on comprehensive literature reviews. In addition, several key parameters of the FLame ~~model-v1.0~~, highlighted in Table 1, were adjusted by calibrating the model based on observations of lake C fluxes (i.e., F_{PP} , diffusive and ebullitive CH_4 emissions). For instance, the parameters $P_{Chl,max}$ and $K_{s,P}$ control the lake primary production and were tuned to reproduce broad global patterns of primary production rates across the full range of lake trophic status (Wetzel, 2001). The mineralization k_{20} and burial constants k_{bur} were adjusted based on the observed fraction of $C_{OC,auto}$ that settles onto the lake sediment, either to be decomposed in ~~an aerobic~~anaerobic or oxic conditions or accumulated in the sediment (Hanson *et al.*, 2011, 2014; Maavara *et al.*, 2019; Mendonça *et al.*, 2017). The temperature dependence of mineralization θ was fine-tuned to reproduce the observational ranges of temperature dependence of net- CH_4 emissions (Aben *et al.*, 2017). f_{mm} specifies the fraction of mineralization that channels to the methanogenesis pathway, which is adjusted to produce the observational patterns of CH_4 emissions. α_{min} is the base value of the exponentially decreasing rate of CH_4 production versus sediment depth, and controls the split of CH_4 production between diffusive and ebullitive pathways, which was calibrated to reproduce observed broad trends of F_{tot} , F_{ebul} and F_{diff} from the literature (Rinta *et al.*, 2017). The parameter values listed in Table 1 provide the reference setup for the simulation of lake CH_4

emissions, and the sensitivity and uncertainty analyses regarding the key model parameters
(~~listed~~indicated by asterisks in Table 31) is carried out using wide ranges of values covering most
possible lake conditions from the real world (see section 3.3.3).

2.4 Numerical solution

In FLame-v1.0, the physical (i.e., CSLM) and biogeochemical (OC, CH₄ and O₂) modules are
coupled online. For the dynamics of volume-integrated OC and CH₄ in sediments, the involved
ordinary differential equations are solved using a forward Euler scheme. For the dynamics of
dissolved O₂ and CH₄ concentrations in the water column, the partial differential equations (Eqs.
(18) and (23)) are solved numerically using an explicit central difference scheme for depth and Euler
forward scheme for time. The diffusion coefficient K_{diff} for both O₂ and CH₄ is ~~set as~~ depth-
dependent (Table 1) to capture the reduced transport when the temperature gradient from the
epilimnion, metalimnion and hypolimnion is well pronounced (Dong et al. 2020; Imboden and
Wuest 1995; Imberger 1985; Boehrer and Schultze 2008).

Table 1. Model parameters of FLAME v1.0 and the choice of their values

Main processes	Key model parameters	Physical meanings (units)	Values	Ranges	Equations	References	插入的单元格
Lake morphology	s	Steepness of lakebed (-)	2	<u>/</u>	(1)	-	
Primary production	$P_{chl,max}$	Maximum carbon fixing rate per unit of Chlorophyll-a (mg C (mg Chl-a) ⁻¹ h ⁻¹)	0.5*	<u>0.5–6</u>	(3)	Behrenfeld and Falkowski (1997)	
	$K_{s,P}$	Half saturation coefficient of total dissolved phosphorus for the primary production (g m ⁻³)	0.09*	<u>0.006–0.18</u>	(3)	Maavara <i>et al.</i> , (2017)	
	$Q_{10,prod}$	Temperature sensitivity for the primary production	2	<u>1.8–2.25</u>	(4)	Lewis (2001) and Reynolds (2006)	
	k_c	Absorbance of PAR per unit of chlorophyll-a (m ² (g Chl-a) ⁻¹)	0.014× 10 ³	<u>(0.01–0.02)×10³</u>	(5)	Lewis (2001) and Reynolds (2006)	
	PP/RP	ratio of maximum gross photosynthesis to respiration per unit chlorophyll-a (-)	15	<u>/</u>	(5)	Lewis (2001) and Reynolds (2006)	
	PAR_k	PAR at the onset of photo saturation (μmol m ⁻² s ⁻¹)	120	<u>90–250</u>	(5)	Lewis (2001) and Reynolds (2006)	
	K_{dw}	PAR attenuations due to pure water (<u>m⁻¹</u>)	0.13	<u>0.12–0.20</u>	(5)	Lewis (2001) and Reynolds (2006)	
Mineralization and burial of organic carbon	K_{dp}	PAR attenuations due to suspended particulate matter (<u>m⁻¹</u>)	0.06	<u>0.05–4</u>	(5)	Lewis (2001) and Reynolds (2006)	
	k_{20}	Mineralization rate at a reference temperature of 20 °C (d ⁻¹)	0.008*	<u>0.003–0.015</u>	(7)	Maavara <i>et al.</i> , (2017)	
	θ	Temperature dependence of mineralization	1.02*	<u>1.01–1.07</u>	(7)	Maavara <i>et al.</i> , (2017)	

	k_{bur}	Carbon burial rate in the lake (d ⁻¹)	0.004*	<u>1/2k₂₀</u>	(8)	Mendonca <i>et al.</i> , (2017)
	f_{mm}	Fraction of mineralization that channels to the methanogenesis pathway	1/4*	<u>1/6–1/2</u>	(10) and (27)	Hanson <i>et al.</i> (2014); Bastviken (2009)
CH ₄ oxidation	k_{max}	Maximal rate of CH ₄ oxidation (g CH ₄ m ⁻³ d ⁻¹)	0.69	<u>0.19–7.68</u>	(19)	Liikanen <i>et al.</i> (2002)
	$Q_{10,ox}$	Temperature dependence of CH ₄ oxidation (-)	<u>1.2</u>	<u>1.1–2.0</u>	(19)	Liikanen <i>et al.</i> (2002)
	$K_{s,CH4}$	Half-saturation constant for CH ₄ (g CH ₄ m ⁻³)	0.6	<u>/</u>	(19)	Stepanen <i>et al.</i> (2016)
	$K_{s,O2}$	Half-saturation constant for O ₂ (g O ₂ m ⁻³)	0.67	<u>/</u>	(19)	Liikanen <i>et al.</i> (2002)
Shape parameter of sedimentary CH ₄ production	α_{min}	Base value of the exponentially decreasing rate of CH ₄ production versus sediment depth (m ⁻¹)	10*	<u>10–70</u>	(12)	Langenegger <i>et al.</i> , (2019)
Gas transport in the water column and exchange with air	K_{diff}	Depth-dependent eddy-diffusion coefficient (m ² d ⁻¹)	8.64 (epilimnion), 8.64× 10 ⁻³ at the thermocline, and 8.64×10 ⁻¹ (hypolimnion)	<u>8.64×10⁻²–1.728</u>	(18) and (23)	Stefan and Fang (1994)
	C_{kl}	Empirical constant for piston velocity (m s ⁻¹)	5.75×10 ⁻⁶	<u>/</u>	(33)	Cole and Caraco, (1998)
	C_{k2}	Empirical constant for piston velocity (m s ⁻¹)	5.97×10 ⁻⁷	<u>/</u>	(33)	Cole and Caraco, (1998)
	n	Empirical constant for piston velocity	1.7	<u>/</u>	(33)	Cole and Caraco, (1998)
	$S_{c,CH4}$	Schmidt number of CH ₄ (-)	677	<u>/</u>	(33)	Wanninkhof <i>et al.</i> (2009)

	S_{c,O_2}	Schmidt number of O ₂ (-)	589	/	(33)	Wanninkhof <i>et al.</i> (2009)
	$f_{CH_4,atm}$	Atmospheric molar fractions of CH ₄	0.18×10^{-13}	/	(31)	Lan <i>et al.</i> (2024)
	$f_{O_2,atm}$	Atmospheric molar fractions of O ₂	0.2095	/	(32)	Gatley <i>et al.</i> (2008)

566

567

568

* indicates that the original parameter values are from the literature, and further adjusted by calibration versus observations. Moreover, their values are varied for the sensitivity analysis in section 3.3.3.

/ indicates that the ranges of the parameter values are not reported.

569 2.5 Case studies

570 We implemented three case studies to assess the performance of FLaMe-[v1.0](#) in simulating lake
571 CH₄ emissions, as well as its application to the European scale. First, we present theoretical
572 simulations for two representative cases (methodological details in section 2.5.1) to assess the general
573 behaviors of FLaMe-[v1.0](#) in capturing the physical-biogeochemical patterns of contrasted lakes. Then,
574 we perform the simulations for four well-surveyed real lakes to assess the model's capability in
575 capturing the observed temporal variations of CH₄ fluxes (section 2.5.2). Next, we apply FLaMe-[v1.0](#)
576 to the entire European domain to assess the model's capability in reproducing the spatial patterns and
577 seasonal variations of CH₄ fluxes at continental scale (section 2.5.3). The European scale application
578 can be considered as a “proof of concept” in support of our proposed modeling strategy. Finally, we
579 examine the sensitivity to key model parameters and assess the uncertainty of the continental-scale
580 emissions using the samples produced by sensitivity analysis, combined with a machine learning
581 approach (section 2.5.4).

582 2.5.1 Two theoretical representative lakes for testing FLaMe-[v1.0](#) performance

583 To test if the FLaMe-~~model~~-[v1.0](#) can capture the contrast [patterns](#) in physical-biogeochemical
584 behaviors across shallow vs. deep, eutrophic vs. oligotrophic and warm vs. cold lakes, we set-up the
585 model for two theoretical representative lakes: a “deep oligotrophic” lake ($h_{max} = 35$ m or $h_{mean} = 17.5$
586 m and $[TP] = 3 \mu\text{g P L}^{-1}$) driven by a “cold” climate (63.75°N , 26.25°E ; Fig. S1) and a “shallow
587 eutrophic” lake ($h_{max} = 10$ m or $h_{mean} = 5$ m and $[TP] = 80 \mu\text{g P L}^{-1}$) driven by a “warm” climate
588 (43.75°N , -6.25°E ; Fig. S2). [The lake areas of these two theoretical lakes were set as 5 km², which](#)
589 [was tested to have limited effects on the simulation results.](#) For these two theoretical representative
590 cases, FLaMe-[v1.0](#) simulates the spatio-temporal evolutions of physical and biogeochemical

591 variables and fluxes, including primary production and mineralization fluxes, and labile
592 autochthonous OC stocks as well as the vertically resolved gradients of temperature, CH₄ and O₂
593 concentrations. Furthermore, we also compared the seasonal patterns of CH₄ productions and
594 emissions for these two ~~contrast~~contrasting lakes. To investigate further how environmental factors
595 affect the ~~FLaMe~~ model behavior, we further decompose the collective responses of shallow and deep
596 lakes into individual effects induced by trophic level, climate (Fig. S1–S3) and lake depth using
597 hypothetical numerical simulations, i.e., (i) changing the maximal lake depth (h_{max}) from 5 to 25 m;
598 (ii) increasing the [TP] levels from 8 to 80 $\mu\text{g P L}^{-1}$; and (iii) changing the climate from warm
599 (43.75°N, -6.25°E; Fig. S1) to cold conditions (63.75°N, 26.25°E; Fig. S2).

600 2.5.2 Simulations of temporal patterns for four well-surveyed lakes

601 To evaluate the ability of FLaMe-v1.0 to reproduce the observed temporal patterns of CH₄ fluxes,
602 we selected four lakes from the Inter-Sectoral Impact Model Intercomparison Project (ISIMIP) lake
603 datasets for which monthly resolved temporal CH₄ fluxes were available: ~~(Tan et al., 2024)~~. These
604 lakes cover different lake depths, areas, climate conditions and trophic statuses, as summarized in
605 Table 2. Since *in-situ* measurements of climatic drivers are not available for these lakes, we extracted
606 them from the 0.5°x0.5° GSWP3-W5E5 global climate forcings released by the ISIMIP3a project as
607 an approximation. The measurements of CH₄ fluxes for these lakes were mostly collected during the
608 first 20 years of the 21st century, and we thus selected the climate forcings for the period 1991–2019,
609 using the period 1991–1999 as spin-up phase. Since the lack of ~~concomitant in-situ measured~~
610 ~~measurements of~~ climatic drivers, ~~as well as observations of~~ and variations in lake water levels ~~and~~
611 ~~areas~~, affect the model's ability to capture the full variability in the time-series of observed CH₄
612 emission time series, we here focus only your evaluation on the magnitudes and broad seasonal patterns

in observed CH₄ emissions, [following what can be achieved for regional and global scale applications](#).
 Thus, we evaluated the simulated statistics (mean and SD represented by boxplots) of CH₄ fluxes
~~within~~ [over](#) the [yearannual cycle](#) against the observational data.

Table 2. Characteristic information for the four well-surveyed lakes from ISIMIP datasets

Lake	Coordinates	Lake depth	Lake area (km ²)	Climate	Trophic status	DataTemporal coverage	Spatio-temporal resolution
Klöntal	47.026N, 8.981E	21.4m (mean), 45m (max)	2.25	Temperate	Oligotrophic	Annual mean	Site; monthly
Erssjön	58.371N, 12.162E	1.3m (mean), 4.75m (max)	0.062	Temperate- Boreal	Mesotrophic	2012–2013	Site; bi-weekly
Upper Mystic	42.434N, 71.150W	11.7m (mean), 25m (max)	0.58	Temperate	Eutrophic	2007–2008	Site; weekly
Villasjön	68.35N, 19.03E	1.3 m (max)	0.17	Boreal	Oligotrophic	2010–2017	Site; daily

插入的单元格

2.5.3 Implementation of [FLaMe-v1.0](#) at continental scale

To implement the model at the scale of Europe (25°W–60°E, 36°–71°N), we extracted the
[natural](#) lakes ([type I](#)) within this domain from the HydroLAKES database (Messenger *et al.*, 2016;
 n=108407, total area = 1.33x10⁵ km² for lakes with 0.1≤*A*₀≤1000 km² within the European domain).
 Following our clustering strategy, we subdivided, within each grid cell, all lakes into four classes
 based on their surface area (0.1 < *A*₀ < 1 km², 1 < *A*₀ < 10 km², 10 < *A*₀ < 100 km², and 100 < *A*₀ < 1000
 km²). As [FLaMe-v1.0](#) was derived from the small lake physics model CSLM, we here only
 considered the lakes with an area smaller than 1000 km², and excluded the very large lakes (*A*₀ > 1000

627 km²) that account for 40% of the total European lake surface area (but only consist of 21 lakes).
628 Within our model domain, we have 108407 lakes with a surface area larger than 0.1 km², which at
629 spatial resolution of 2.5 degree (Fig. S4–S5) result in 365 grid cells and 953 representative lakes
630 (hence reducing computation cost by more than a factor of 100 compared to a case where each
631 individual lake would be simulated). By parallelizing the model simulations on a high-performance
632 cluster, the implementation of FLaMe-[v1.0](#) for the entire European domain consumes approximately
633 365 CPU hours for a single run covering 10 years.

634 The FLaMe-~~model-v1.0~~ was forced by meteorological conditions from the GSWP3-W5E5
635 reanalysis product under ISIMIP3a (Frieler *et al.*, 2024) (Fig. S6), including shortwave solar
636 radiation (W m⁻²), longwave solar radiation (W m⁻²), precipitation (mm s⁻¹), near surface air
637 temperature (at 10 m height, °C), specific humidity (kg kg⁻¹), near surface wind velocity (at 10m, m
638 s⁻¹), and atmospheric pressure (Pa). As these forcings were provided at a finer spatial resolution of
639 0.5°, we only applied the values in the central 0.5° grid cell of our larger 2.5° grid. In addition, the
640 FLaMe-~~model-v1.0~~ was also driven by the [TDPTP](#) in the representative lakes (Fig. S7–S8), which
641 was estimated by dividing the [TDPTP](#) mass outflow by the water discharge reported in
642 HydroLAKES, hence assuming that the lake water is well mixed. The TP mass outflow from each
643 lake in HydroLAKES was obtained by routing the TP loads (extracted from the GlobalNEWS model;
644 Mayorga *et al.*, (2010)) from the watershed (point and non-point terrestrial sources) into the river
645 network, following the procedure outlined in Lauerwald *et al.* (2019) and topological information
646 provided by the HydroSHEDS drainage network. More details related to the TP routing can be found
647 in Bouwman and Billen (2009), Van Drecht *et al.* (2009), and Mayorga *et al.* (2010).

648 To validate the FLame-v1.0 for European lakes, we will evaluate the simulated F_{PP} and CH_4
649 emission rates against the ranges/values reported in the literature and/or from observations. First,
650 the simulated F_{PP} will be evaluated against empirical ranges reported by Wetzell (2001) for lakes
651 from ultraoligotrophic (0–5 $\mu\text{gP L}^{-1}$), oligotrophic (5–10 $\mu\text{gP L}^{-1}$), mesotrophic (10–30 $\mu\text{gP L}^{-1}$), to
652 eutrophic ($>30 \mu\text{gP L}^{-1}$) conditions. Next, the simulated diffusive and ebullitive CH_4 emission rates
653 will be evaluated against *in-situ* measurements compiled by Rinta et al. (2017) from 17 boreal lakes
654 (in southern Finland and Sweden) and 30 central European lakes (in The Netherlands, Germany and
655 Switzerland). This dataset is adopted because it can not only differentiate the ebullitive and diffusive
656 CH_4 fluxes during late summer (August and September, 2010–2011) but also provides information
657 regarding environmental conditions of the study area (mean annual air temperature, annual
658 precipitation, percentage of forests and managed land in the catchment) and water chemistry of the
659 studied lakes (temperature, conductivity, pH, absorbance, TP and TN in surface water, and average
660 TP and TN in the water column), which are helpful for understanding the lake methane dynamics
661 within these two contrasted regions. However, this dataset of 47 lakes still has some important
662 limitations, in particular as it presents only summer-time observations, and not time-series which
663 would comprise the full seasonal cycle including turnover events and other hot moments. In addition,
664 it contains potential biases induced by the calculation methods used for separating the measured
665 CH_4 fluxes into diffusive and ebullitive pathways. In particular, Rinta et al. (2017) used floating
666 chambers over a relatively short duration (6hr), which might not be able to detect sporadic ebullition
667 events, and did not employ bubble traps to estimate the ebullitive flux.

668 2.5.4 Sensitivity and uncertainty analysis

669 To explore how model parameterization affects the European-scale assessments of lake CH₄
670 emissions, we conducted a sensitivity analysis encompassing the parameters whose variations
671 induce the largest changes in lake CH₄ dynamics ~~and listed~~(with the involved parameters indicated
672 ~~by asterisks~~ in Table 3-1). The sensitivity was conducted by varying a parameter once at a time: only
673 one parameter is varied with the other parameters kept unchanged. All these parameters were
674 assumed to have Gaussian distributions, with their SDs specified as 50% of their original values,
675 except the temperature dependency $Q_{10,ox}$ and θ whose SDs were specified as 50% of their deviation
676 to unity. More specifically, we tested the sensitivity within the ranges of mean \pm SD at four points,
677 i.e., +SD, +0.5SD, -0.5SD, and -SD.

678 To constrain uncertainties in European scale CH₄ emissions, we complemented the sensitivity
679 analysis (n=36) with another 28 scenarios under several extreme cases and different combinations
680 of variations in key parameters. With these 64 assessments taken as samples, we then used a machine
681 learning approach to assess the uncertainty associated ~~to~~with our estimation of European lake CH₄
682 fluxes. Specifically, we trained a Random Forest (RF) model that capture nonlinear relationships
683 between our key model parameters and European lake CH₄ emissions, i.e., the key parameters are
684 taken as predictors and the European lake CH₄ emissions are taken as target variable. Next, we
685 produced 1000 Gaussian-distributed random samples within the parameter space and estimated an
686 ensemble of CH₄ emissions using the trained RF model.

Table 3 Key model parameters selected for sensitivity and uncertainty analysis

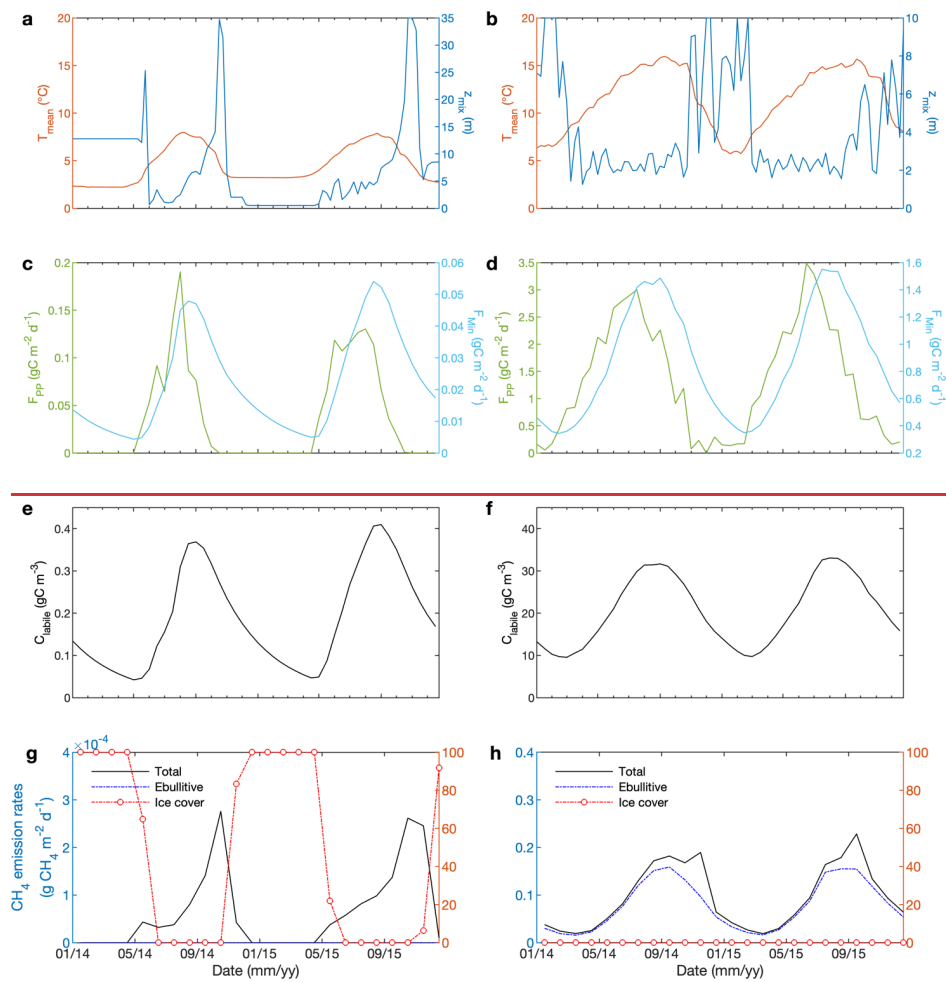
Main processes	Key model parameters	Physical meanings (units)	Values	Ranges	Eq.	References
Primary production	$P_{chl,max}$	Maximum carbon fixing rate per unit of Chlorophyll-a ($\text{mg C (mg Chl-a)}^{-1}\text{h}^{-1}$)	0.5	0.5–6	(3)	Behrenfeld and Falkowski (1997)
	$K_{s,p}$	Half saturation coefficient of total dissolved phosphorus for the primary production (g m^{-3})	0.09	0.006–0.189	(3)	Maavara <i>et al.</i> , (2017)
Mineralization and burial of organic carbon	k_{20}	Mineralization rate at a reference temperature of 20 °C (d^{-1})	0.008	0.003–0.015	(7)	Maavara <i>et al.</i> , (2017)
	θ	Temperature dependence of mineralization	1.02	1.01–1.07	(7)	Maavara <i>et al.</i> , (2017)
	k_{bur}	Carbon burial rate in the lake (d^{-1})	0.004	$1/2k_{20}$	(8)	Mendonça <i>et al.</i> , (2017)
	f_{mm}	Fraction of mineralization that channels to the methanogenesis pathway	1/4	1/6–1/2	(10) (26)	Hanson <i>et al.</i> (2014); Bastviken (2009)
CH ₄ oxidation	k_{max}	Maximal rate of CH ₄ oxidation ($\text{g CH}_4\text{m}^{-3}\text{d}^{-1}$)	0.69	0.19–7.68	(18)	Liikanen <i>et al.</i> (2002)
	$\theta_{0,ox}$	Temperature dependence of CH ₄ oxidation (–)	1.2	1.1–2.0	(18)	Liikanen <i>et al.</i> (2002)
Base value of the shape parameter	α_{min}	Exponentially decreasing rate of CH ₄ production versus sediment depth (m^{-1})	10	10–70	(12)	Langenegger <i>et al.</i> , (2019)

689

690 3. Results

691 3.1 Assessing the performance of FLaMe-v1.0 in capturing patterns of CH₄ dynamics across 692 different lake types

693 The FLaMe-model-v1.0 is shown to be able to well capture the typically observed, contrasting
694 physical and biogeochemical behaviors for two representative cases (Fig. 5 and Fig. S9–17; more
695 details in Supplementary Text S3): shallow vs. deep, eutrophic vs. oligotrophic and warm vs. cold
696 lakes. In the deep oligotrophic lake, the mean temperature reveals a lower and narrower seasonal
697 variability ($\sim 3\text{--}8^\circ\text{C}$) compared to the shallow eutrophic lake ($5\text{--}15^\circ\text{C}$) (Fig. 5a vs. 5b). Large
698 temperature variations in the latter are mainly driven by the smaller water volume and thus faster
699 mean temperature response to fluctuations in atmospheric temperature. In addition, the annual
700 averaged F_{PP} in the shallow eutrophic lake ($490\text{ gC m}^{-2}\text{ yr}^{-1}$) is approximately 38 times higher than
701 that in the deep oligotrophic lake ($13\text{ gC m}^{-2}\text{ yr}^{-1}$) (Fig. 5c vs. 5d). This difference can be explained
702 by the differences in water volume (energy exchange), trophic status, and climate forcings. The higher
703 F_{PP} of the shallow eutrophic lake also translates into higher $C_{OC,auto}$ concentration (~ 110 times) which
704 persist over longer periods (Fig. 5e vs. 5f), despite substantially higher F_{min} rates.



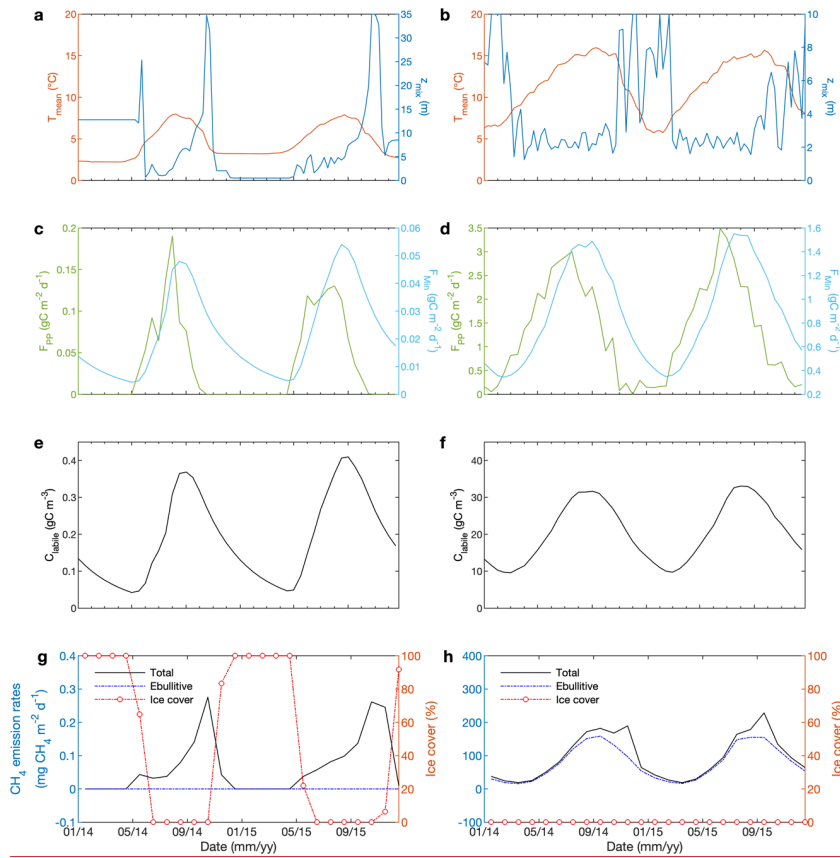


Fig. 5. Depth-integrated temporal evolution of variables and processes in two theoretical representative lakes. The deep oligotrophic lake (left) has a maximal depth of 35 m and $[TDP_{TP}]$ of $3 \mu\text{gP L}^{-1}$, and is driven by the climate forcings at the location of 63.75°N , 26.25°E . The shallow eutrophic lake (right) has a maximal depth of 10 m and $[TDP_{TP}]$ of $80 \mu\text{gP L}^{-1}$, and is driven by the climate forcings at the location 43.75°N , -6.25°E . (a) and (b) show the evolution of lake mean temperature and mixing depth; (c) and (d) show the evolution of primary production (F_{PP}) and mineralization rate (F_{Min}); (e) and (f) show the evolution of concentration of

713 autochthonous organic carbon ($C_{OC,auto}$); (g) and (h) show the evolution of CH_4 emission rates and ice cover.
714 Note the difference scales between the left and right panels.

715 In the deep oligotrophic lake, the simulated vertical temperature profiles indicate an almost
716 permanently maintained stratification that is only interrupted by short but intense turnover events
717 during late falls (Fig. S9a). Lake stratification (e.g., lake turnover and O_2 concentrations that depend
718 mostly on solubility and hence, temperature) dominates the spatio-temporal pattern of O_2 such that
719 O_2 concentration is near-saturated during most of the year (Fig. S9c). The oligotrophic status, together
720 with the well oxygenated conditions, results in extremely low CH_4 concentrations. Higher CH_4
721 concentrations are only simulated near the lake bottom following the productive season, i.e., late
722 summer/fall transition (Fig. S9e). In contrast, in the shallow eutrophic lake, the weaker stratification
723 results in a less pronounced vertical temperature gradient (Fig. S9b). The vertical lake O_2 profile is
724 not only controlled by the lake physics (temperature and O_2 solubility) but also by intense
725 biogeochemical processes (Fig. S9d). During summer, O_2 concentrations in the upper portion of the
726 lake are slightly supersaturated due to photosynthetic activity, followed by a gradual decrease in O_2
727 concentration as mineralization rates exceed primary production rates. Due to the high primary
728 production in the eutrophic lake, large amounts of OC are exported below the thermocline, where
729 heterotrophic activity progressively depletes O_2 , leading to the development of anoxic conditions in
730 the hypolimnion. The combination of high F_{Min} and low O_2 concentrations drive the accumulation of
731 CH_4 in late summer at the bottom of the lake (Fig. S9f), with maximal CH_4 concentration ($3.0 \text{ g } CH_4$
732 m^{-3}) exceeding those simulated in the deep oligotrophic lake by a factor of 600 (Fig. S9e).

733 By aggregating CH₄ fluxes over time, we obtained distinct seasonal patterns of CH₄ production
 734 and emission for these two representative lakes (Fig. 5g and 5h; Fig. S10). In the cold, deep
 735 oligotrophic lake (Fig. 5g and Fig. S10a), winter to early spring ice cover (December–April) blocks
 736 CH₄ emissions such that lake CH₄ emissions are limited to the period between May and November.
 737 CH₄ production is highest (~~0.8×10⁻⁴ g~~ mg CH₄ m⁻² d⁻¹) in August and lowest (~~8.0×10⁻⁵ g~~ 0.08 mg
 738 CH₄ m⁻² d⁻¹) in April. Almost all the produced CH₄ escapes the sediment via diffusion as gas bubbles
 739 do not form due to low CH₄ production rates and high-water pressure. However, the benthic CH₄ flux
 740 is subsequently largely oxidized in the well oxygenated deep water column. As a result, total lake
 741 CH₄ emissions are low (0 to ~~2.4×10⁻⁴ g~~ 0.24 mg CH₄ m⁻² d⁻¹) with a slight peak in October. In the
 742 shallow eutrophic lake (Fig. 5h and Fig. S10b), the warmer climate prevents ice formation on the lake
 743 surface, leading to an emission season about twice as long as under colder climatic conditions. CH₄
 744 production (~~0.0220~~ to ~~0.35 g~~ 350 mg CH₄ m⁻² d⁻¹) is >1000 times higher than that in cold, deep
 745 oligotrophic lake due to the higher nutrient loads, lower O₂ levels, higher irradiance as well as higher
 746 temperature (Fig. 5b). Higher CH₄ production rates, together with lower water pressure, drive the
 747 formation of gas bubbles, leading to a higher fraction of CH₄ emissions via the ebullitive pathway.
 748 The weaker stratification and the shorter transport time scale in the shallow lake limits CH₄ oxidation
 749 during diffusive transport, leading to ~900 times higher total CH₄ emissions compared to the deep,
 750 oligotrophic lake. Total lake CH₄ emissions are highest (~~0.21 g~~ 210 mg CH₄ m⁻² d⁻¹) in September and
 751 lowest (~~0.02 g~~ 20 mg CH₄ m⁻² d⁻¹) in February.

752 By decomposing the collective responses of shallow and deep lakes into individual effects
 753 induced by trophic level, climate and lake depth using additional theoretical numerical simulations,
 754 we found that the trophic level exerts the most important control on CH₄ dynamics, followed by

755 climate, and finally, lake depth (Fig. S11–S14). Specifically, the yearly mean CH₄ production is
756 increased by a factor of 30 (from ~~0.0033~~ to ~~0.089~~ **g89 mg** CH₄ m⁻² d⁻¹), and the yearly mean CH₄
757 emission is increased by a factor of 44 (from ~~0.00131.3~~ to ~~0.057~~ **g57 mg** CH₄ m⁻² d⁻¹) from
758 oligotrophic to ~~trophie~~**eutrophic** status (i.e., [TDP] increased by 10 times) (Fig. S12). From cold to
759 warm climate, the yearly mean CH₄ production and emission increase by a factor of 6 (~~0.00949.4~~ to
760 ~~0.059~~ **g59 mg** CH₄ m⁻² d⁻¹) (Fig. S13), and a factor of 5 (~~0.00575.7~~ to ~~0.0330~~ **g** CH₄ m⁻² d⁻¹),
761 respectively. By increasing lake depth from 15 m to 35 m (Fig. S14), the CH₄ production rates remain
762 almost the same, i.e., ~~0.02~~ **g20 mg** CH₄ m⁻² d⁻¹ for the yearly mean and ~~0.06~~ **g60 mg** CH₄ m⁻² d⁻¹ for
763 the peak, while the CH₄ emissions are overall lower (~~35 to 22 mg CH₄ m⁻² d⁻¹ for the peak without~~
764 ~~considering the storage flux~~) for the deeper lake.

765 3.2 Evaluation of simulated temporal lake CH₄ emissions against observations from four well- 766 surveyed lakes

767 In Klöntal and Erssjön Lakes (Table 2, Fig. 6a and 6b), FLaMe-~~v1.0~~ captures the observed
768 seasonal cycles of CH₄ emissions well, albeit with almost a one-month delay. As a result, the
769 simulated CH₄ fluxes are slightly lower in the first half of the year and slightly higher in the second
770 half. This lag between observations and model results is likely due to the use of idealized climate
771 forcings but could also be attributed to the unresolved changes in water levels and in-lake TDP
772 dynamics. In the Klöntal Lake (Fig. 6a), the observed CH₄ fluxes are exceptionally high in April (1.64
773 ~~gmg~~ CH₄ m⁻² d⁻¹) and July (5.03 ~~gmg~~ CH₄ m⁻² d⁻¹), interrupting the normal seasonal cycles. These
774 abrupt observed emissions might reflect the contributions from storage fluxes that are not well
775 captured by FLaMe-~~v1.0~~. Apart from these two months with exceptionally high fluxes, the
776 observational data indicates peak emissions of 3.18 ~~gmg~~ CH₄ m⁻² d⁻¹ in August and no emissions

777 during the ice-covered period. FLAME-v1.0 simulates similar fluxes, with a peak of 3.4 $\text{gmg CH}_4 \text{ m}^{-2} \text{ d}^{-1}$ in September (and 3.17 $\text{gmg CH}_4 \text{ m}^{-2} \text{ d}^{-1}$ in August), and a null flux in January–February when
 778 the model predicts ice formation. In the Erssjön Lake (Fig. 6b), observational data report a peak in
 779 CH_4 emission reaching 13.48 $\text{gmg CH}_4 \text{ m}^{-2} \text{ d}^{-1}$ in July and no emissions during the ice-covered period,
 780 whereas FLAME-v1.0 simulates a peak emission of 18.76 $\text{gmg CH}_4 \text{ m}^{-2} \text{ d}^{-1}$ in August (and 12.82 gmg
 781 $\text{CH}_4 \text{ m}^{-2} \text{ d}^{-1}$ in July), and no flux in February. Moreover, the simulated CH_4 fluxes are exceptionally
 782 high in April (11.10 $\text{gmg CH}_4 \text{ m}^{-2} \text{ d}^{-1}$) due to the release of a storage fluxes that does not seem to be
 783 recorded by the observations. These high CH_4 fluxes attributed to storage and lake turnover are
 784 usually associated with large variability, i.e., in Klöntal Lake (Fig. 6a), the observed variability
 785 (standard deviation, SD) in CH_4 flux in July is almost 8-fold larger than the simulated one, whereas
 786 in Erssjön Lake (Fig. 6b), the simulated SD in CH_4 flux in April is almost 6-fold larger than that of
 787 the observed one. This suggests that both *in-situ* measurements and FLAME-v1.0 struggle to
 788 accurately capture the storage fluxes. Apart from these storage fluxes, we found that the SDs of CH_4
 789 fluxes simulated by FLAME-v1.0 are lower than those observed for most months, indicating a more
 790 stable behavior in the simulations compared to the observations across the multi-year period
 791 considered here.

793 For the Upper Mystic and Villasjön Lakes (Fig. 6c and 6d), the observed temporal patterns of
 794 CH_4 fluxes appear more erratic, either due to the dominant role of short-term water level fluctuations
 795 or due to the complex ice cover dynamics. For the Upper Mystic Lake (Fig. 6c), the observed CH_4
 796 fluxes are irregular or fluctuating (0–17.6 $\text{gmg CH}_4 \text{ m}^{-2} \text{ d}^{-1}$) over the year, a pattern which was
 797 explained by dynamic variations of lake water levels (Varadharajan, 2009). Since *in-situ* water level
 798 measurements are lacking and the lake area and depth are set as constant in the model, the simulated

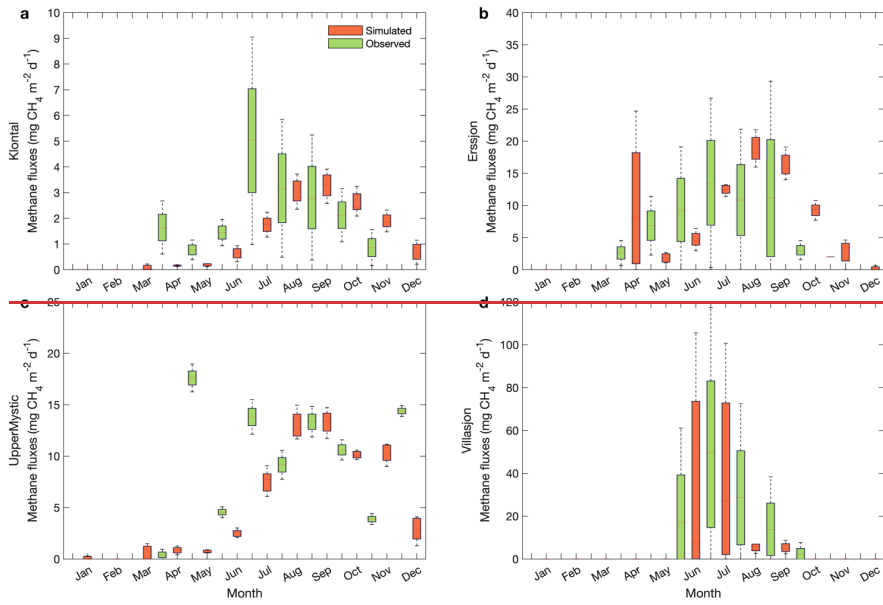
799 temporal variations cannot capture these observed erratic patterns well. Our model produces a
800 smoother seasonal cycle of monthly-mean CH₄ fluxes over the year, i.e., high fluxes (10.02–13.38
801 [gmg](#) CH₄ m⁻² d⁻¹) during the productive season (August–October), and low fluxes (0.02–7.56 [gmg](#)
802 CH₄ m⁻² d⁻¹) during the other months. Moreover, the model predicts a weak storage flux occurring in
803 November (10.20 [gmg](#) CH₄ m⁻² d⁻¹). For the Villasjön Lake (Fig. 6d), the observed CH₄ fluxes are
804 limited to the period of June–October, due to the long ice cover period induced by the cold climate.
805 FLAME-[v1.0](#) captures the observed ice-cover period well and produces similar seasonal cycles of CH₄
806 fluxes. The simulated means and SDs are very close to observations in June and July, but both, means
807 and SDs, are much lower than observations in August, September, and October.

808 In summary, despite the use of idealized climatic forcing and neglecting variations in lake area
809 and water level, FLAME-[v1.0](#) broadly captures the observed temporal patterns of monthly mean
810 emissions, albeit sometimes with small delays or diverging extents of high emissions periods. The
811 SDs of simulated CH₄ fluxes are also usually lower than the observed values, which is to be expected
812 considering that our model is not designed to capture high-frequency fluctuations of CH₄ fluxes. The
813 largest biases can be found in the estimations of storage fluxes (timing and magnitude), probably due
814 to 1) the difficulty of capturing these fluxes with existing measurement instruments and techniques,
815 2) the possibility of methane oxidation with greater than expected values during turnover and ice-out
816 (Mayr *et al.*, 2020; Zimmermann *et al.*, 2019; Pajala *et al.*, 2022) and 3) the lack of *in-situ*
817 measurements of climate conditions, dynamical water levels, and dynamic TDP concentrations
818 (Denfeld *et al.*, 2018). Resolving these issues will require to assemble a much larger dataset of
819 observed long time-series of CH₄ fluxes and associated physical and biogeochemical variables-, [such](#)
820 [as those reported by Velasco *et al.* \(2024\) and Natchimuthu *et al.* \(2016\).](#) To help further calibrate

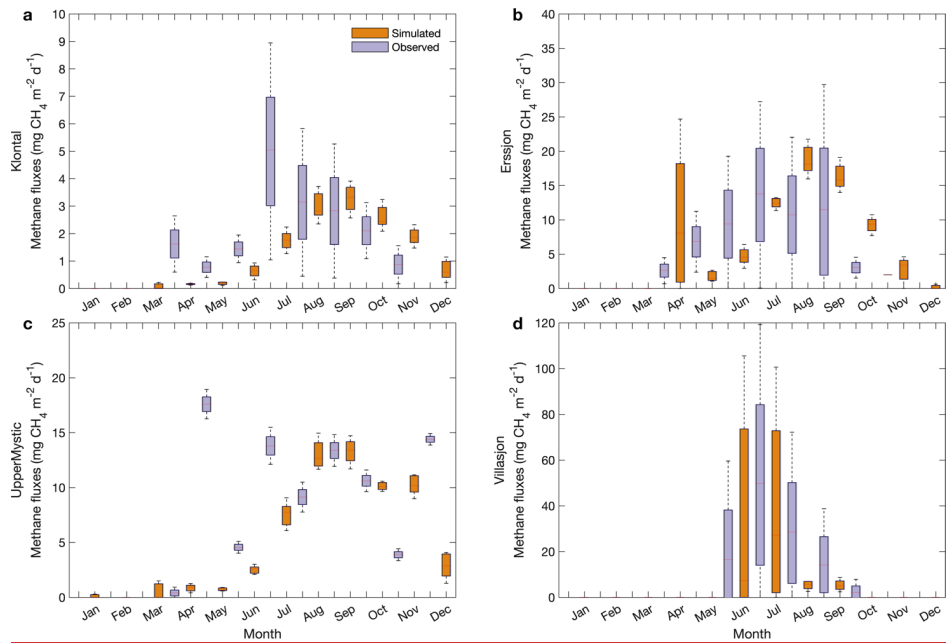
821 and evaluate the model, this much larger pool of observations should span a broader range of
822 environmental conditions to be more representative of the lake CH₄ dynamics on the continental to
823 global scales. Overall, given the scarce spatiotemporal observations and the limited possibility to
824 validate current knowledge on process regulation in fields, it is difficult for all existing models to
825 produce the details of the CH₄ dynamics in specific single lakes. Hence, the temporal patterns of CH₄
826 fluxes simulated by FLAME-v1.0 are seen as acceptable, as its main focus is to capture the broad
827 spatio-temporal patterns of CH₄ emissions across the thousands of lakes that need to be accounted for
828 in large-scale applications (see section 3.3).

829

830



831



832 Fig. 6. Evaluation of FLaMe-v1.0 against monthly mean CH₄ fluxes recorded in long time-series of
 833 observations in four real lakes. (a) Klöntal, (b) Erssjön, (c) Upper Mystic, and (d) Villasjön. The detailed
 834 lake characteristics are listed in Table 2. The climate forcings for these four lakes are extracted from
 835 GSWP3-W5E5 model from ISIMIP3a. Note the different scales of CH₄ emissions in each lake.

836 3.3 FLaMe-v1.0 application on the European domain

837 3.3.1 Evaluation of FLaMe-v1.0 in European lakes

838 In the European scale application of FLaMe-v1.0, we first evaluated the simulated F_{PP} against
 839 the empirical ranges reported by Wetzell (2001) for lakes under ultraoligotrophic (0–5 $\mu\text{gP L}^{-1}$),
 840 oligotrophic (5–10 $\mu\text{gP L}^{-1}$), mesotrophic (10–30 $\mu\text{gP L}^{-1}$), and eutrophic ($>30 \mu\text{gP L}^{-1}$) conditions
 841 (Fig. 7 and Fig. S18). Figure 7 shows that, under different trophic status, the means and medians of
 842 F_{PP} simulated by FLaMe-v1.0 (for 953 representative lakes) fall well within the reported ranges.
 843 Slight deviations could only be observed in ultraoligotrophic lake for which the model tends to
 844 slightly overestimate F_{PP} (Fig. 7a). Ultraoligotrophic and oligotrophic lakes reveal very similar mean
 845 and median of F_{PP} that fall at the higher ends of the ranges specified by Wetzel (2001) or even exceed
 846 it in the case of ultraoligotrophic lakes. In turn, mesotrophic and eutrophic lakes reveal mean and
 847 median F_{PP} that fall at the lower ends of the ranges specified by Wetzel (2001). This slight difference
 848 of simulated versus observed F_{PP} in lakes with different trophic conditions can be explained by the
 849 relatively low value of $K_{s,P}$ (90 $\mu\text{g L}^{-1}$) compared to the concentration of [TDPTP] (Fig. S7–S8), as
 850 well as the simplified representation of lake primary production in our model. When extending the
 851 representative lakes to all real lakes in the European domain ($n=108407$), the median and mean of
 852 simulated F_{PP} are still within the specified ranges but are reduced slightly for all trophic status (Fig.

853 S18), attributed to the positively skewed distribution of [~~T~~DPTP] (Fig. S8), i.e., many lakes have a
854 low [~~T~~DPTP].

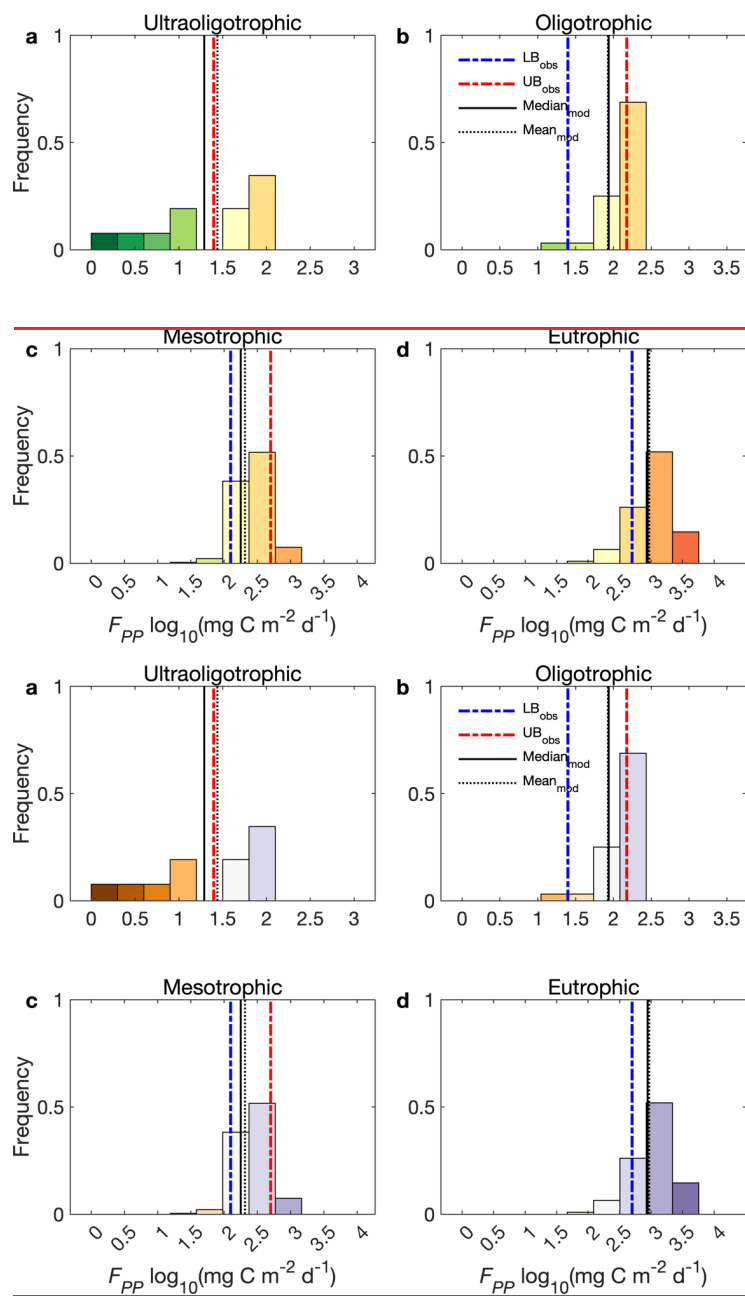
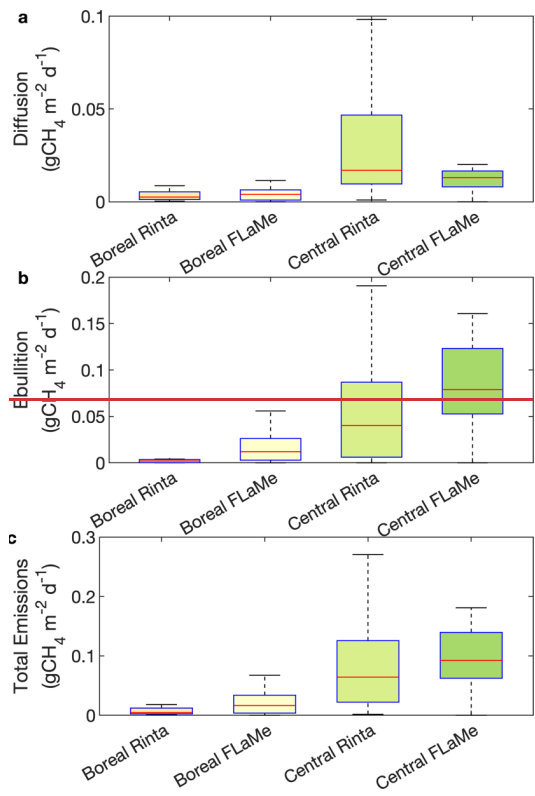


Fig. 7. Comparison of simulated primary production (F_{PP}) with empirical estimates reported by Wetzel (2001). The histograms show the frequency distributions of simulated F_{PP} (log scale) for 953 representative lakes that are grouped into ultraoligotrophic ($0-5 \mu\text{gP L}^{-1}$), oligotrophic ($5-10 \mu\text{gP L}^{-1}$), mesotrophic ($10-30 \mu\text{gP L}^{-1}$), and eutrophic ($>30 \mu\text{gP L}^{-1}$) lakes. In the figure, blue and red dashed lines are the lower and upper bounds (LB_{obs} and UB_{obs}), respectively, of empirical ranges reported by Wetzel (2001) in this class of lakes; Black solid and dotted lines are the $\text{median}_{\text{mod}}$ and mean_{mod} , respectively, of simulated F_{PP} for this class of lakes.

Next, we evaluated the simulated diffusive and ebullitive CH_4 emission rates against measurements in boreal and central European regions during late summer (August–September, 2010–2011) synthesized by Rinta *et al.* (2017) (Fig. 8 and Fig. S19). As Rinta *et al.* (2017) compiled *in-situ* measurements of diffusive and ebullitive CH_4 emission rates from 17 boreal lakes (in southern Finland and Sweden) and 30 lakes of central European lakes (in The Netherlands, Germany and Switzerland), we extracted the mean CH_4 emission rates during August–September for representative lakes located in the grid cells corresponding to these two regions. Results indicate that the simulated diffusive CH_4 emissions for boreal European lakes (Fig. 8) agree well with the observations; yet the simulated ebullitive CH_4 emissions are slightly higher than the observations, leading to slightly higher total emissions. For central European lakes, the simulated diffusive CH_4 emissions are slightly lower than the observations, while the simulated ebullitive CH_4 emissions are slightly higher, leading to a good agreement in the total emissions (Fig. 8). Moreover, Rinta *et al.* The slightly higher ebullitive fluxes simulated by FLAME-v1.0 may be attributed to not only the uncertain choice of model

parameters (e.g., α) but also to the systematically lower measured ebullitive fluxes in Rinta *et al.* (2017), where ebullition was separated from diffusion when the measured fluxes produced unreasonably high k_{600} . Moreover, Rinta *et al.* (2017) reported 6 and 27 times higher diffusive and ebullitive fluxes in central Europe, respectively, while our model simulates a smaller contrast of a 3- and 7-fold difference. This smaller contrast in the simulation can likely be explained by the higher variability in measurements, reflecting diverse climate, light and catchment properties in real lakes, while the variabilities in the simulated fluxes are significantly lower, probably due to more homogeneous representations of environmental conditions in the FLaMe-simulations. Specifically, the large differences in measured CH₄ emissions in boreal and central European lakes are attributed to their distinct characteristics, including climate (colder and dryer in the boreal region), light regime (larger absorbance in the boreal region) and catchment properties, in particular land-use (dominance of forests and smaller fraction of managed agricultural land in the boreal region). However, in FLaMe-v1.0, the catchment properties are not fully captured by our sole, simplified indicator of [TDPTP], such that the differences between boreal and central European lakes are underestimated. The coarse resolution of our model also likely reduces the represented range of climate conditions in our simulations compared to those experienced by the sampled lakes. In the meantime, observations are also associated with uncertainties, because measurements were not continuous in time and might thus not be fully representative of the late summer-early fall period, as well as sampling and measuring CH₄ emissions, in particular via the ebullitive pathway, is all but a trivial task. Nevertheless, the above evaluation of FLaMe-v1.0 against observations overall reveals the ability of our model to reproduce broadly observed patterns in primary production and CH₄ emissions observed across distinct trophic status and landscapes.



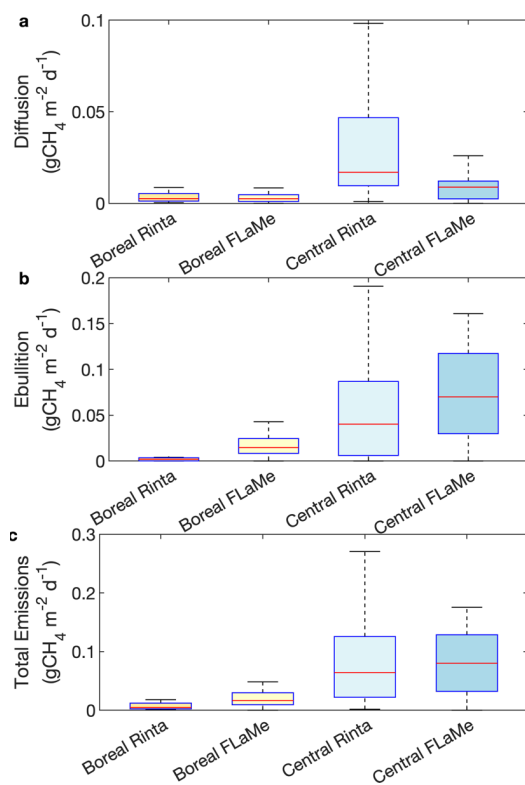


Fig. 8. Comparison of simulated diffusive (top), ebullitive (middle) and total (bottom) CH₄ emission rates with the measurements compiled by Rinta *et al.* (2017). The datasets reported by Rinta *et al.* (2017) comprises the diffusive, ebullitive and total emission rates from 17 boreal lakes in Finland and Sweden and 30 lakes of central European lakes in The Netherlands, Germany and Switzerland. The boxes represent the 25% and 75% quartiles, and the whiskers cover the 95% confidence intervals. The same figure with a log scale is presented in Fig. S19.

3.3.2 European scale assessment of lake CH₄ emissions

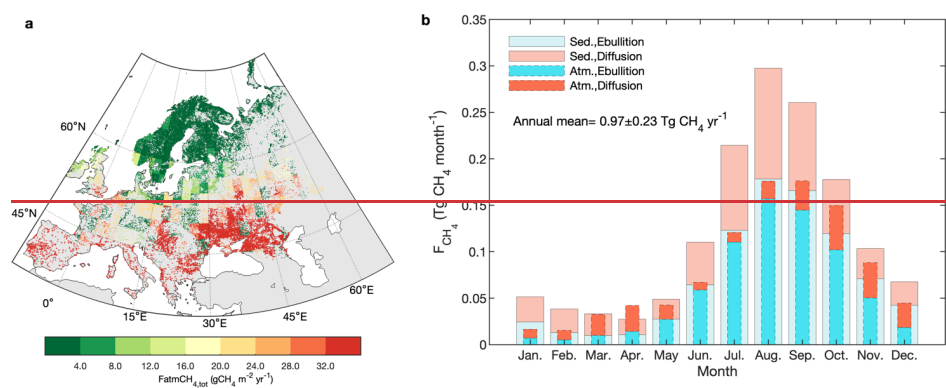
The continental-scale assessment indicates that European lakes smaller than 1000 km² have an annual mean emission of 0.97 Tg CH₄ yr⁻¹ from autochthonous phytoplankton production during the

911 period of 2010–2016, of which 30% and 70% are through diffusive and ebullitive transport pathways,
912 respectively (Fig. 9 and Fig. S20). Note that, by including the estimated emissions from European
913 lakes larger than 1000 km² with two different strategies (Supplementary Text S5), we provide a back
914 of the envelope estimate for the mean total annual emission as 1.03–1.10 Tg CH₄ yr⁻¹, which falls
915 within the lower end of a previously reported range (0.9–2.5 Tg CH₄ yr⁻¹) (Petrescu *et al.* 2023;
916 Lauerwald *et al.*, 2023). The mean CH₄ emission rates per unit lake area amounts to 7.39 g CH₄ m⁻²
917 yr⁻¹, while the mean CH₄ emission rates per unit land surface area amounts to 0.054 g CH₄ m⁻² yr⁻¹.
918 Both emission rates decrease from South to North, despite the larger number of lakes and lake surface
919 area in Northern Europe (Messenger *et al.*, 2016; Fig. S4). This south to north decrease can be
920 explained by a much higher CH₄ emission rate in the South of Europe (reaching 109.6 g CH₄ m⁻² yr⁻¹
921 ¹) driven by much higher eutrophic status of southern lakes (together with higher temperatures), which
922 outcompetes the effect of the larger lake area in the Scandinavian region and Finland (which
923 contribute to ~30% of the European lake area). The ice-cover in northern lakes also contribute to the
924 south-to-north gradient of CH₄ emission rates, which is tested to decrease the European lake
925 emissions by 7%. This latitudinal pattern of CH₄ emissions per unit lake area is broadly consistent
926 with that reported by Johnson *et al.* (2022) based on observations.

927 In terms of seasonal variability, our model results are in full agreement with the sparse data set
928 of seasonally resolved observations (Tan *et al.*, 2015) and show that European lakes as a whole act
929 as a continuous CH₄ source including during the winter months. (individual lakes during ice-covered
930 periods will do not emit CH₄). Moreover, the simulated CH₄ production and emission reveal a sharp
931 10-fold increase from late Spring to late Summer that is largely driven by the increase in ambient
932 temperature and F_{pp} rates. These findings underscore the importance of accounting for seasonal

933 variations in CH₄ emissions when refining regional methane budgets (Tan *et al.*, 2015; Guo *et al.*,
934 2020; Johnson *et al.*, 2022; Stavert *et al.*, 2022). A simple extrapolation of observed summer
935 emissions to the yearly timescale would thus lead to an overestimation of yearly mean fluxes. In
936 addition, model results also reveal a slight time-lag between the most favorable climate conditions
937 (air temperature and light) and the maximum CH₄ production. This time lag in the model can be
938 explained by the cascade of biogeochemical reactions (primary production, mineralization, O₂
939 depletion and onset of CH₄ production) that ultimately control benthic CH₄ fluxes, and the timescale
940 of heat transfer from the lake surface to the deepest portion of our valley-shape lake bottom. This
941 slight time-lag is further amplified by the time required for the benthic CH₄ to reach the water-air
942 interface, although this effect is secondary due to the dominance of shallow lakes (with mean depth
943 <197.8 m for 98.790% of lakes; Messenger *et al.*, 2016) within the European domain. Finally, the
944 broad seasonal pattern in CH₄ emissions is complicated by the episodic releases of storage fluxes
945 during lake turnovers which occur during spring (March and April; emissions>production) and fall
946 (October and November; emission circa 85% of the production). Lake turnovers amplify total
947 emissions for the duration of these short-lived events.

948



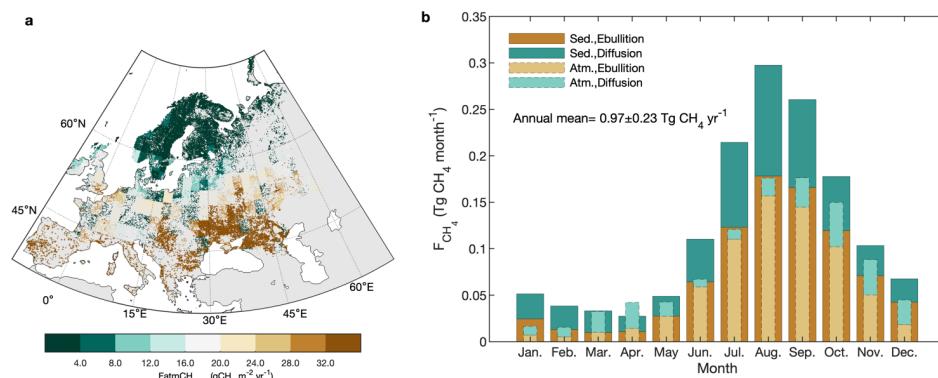


Fig. 9. Methane (CH₄) emissions from European lakes. (a) Spatial distribution of annual mean total CH₄ emissions (sum of diffusion and ebullition) for the period of 2010-2016, expressed in per unit of lake area. (b) Seasonality of total CH₄ production (dashed-colors wide bars with full lines) and emission (full-colors narrow bars with dashed lines) fluxes and their split between ebullitive and diffusive pathways (period 2010-2016).

3.3.3 Sensitivity and uncertainty analysis

The sensitivity analysis of annual mean CH₄ emissions from European lakes to key model parameters (listed indicated by asterisks in Table 31) are summarized in Table 43. Table 43 indicates that the fraction of benthic organic matter mineralization channeled to methanogenesis (f_{mm}) is the most sensitive parameter, and the increase (decrease) of f_{mm} by one SD leads to an increase (decrease) of European lake CH₄ emissions by 0.92 Tg CH₄ yr⁻¹ or 95% (0.67 Tg CH₄ yr⁻¹ or 69%). This is intuitive as a higher fraction of carbon channeled to methanogenesis will increase the continental scale CH₄ emissions, although the response is nonlinear. This is also supported by the findings of high potential methane production rates in various freshwater systems (including the lakes, reservoirs and rivers) (Bodmer *et al.*, 2025). The second and third most sensitive parameters are the maximum carbon fixation rate per unit of Chlorophyll-a ($P_{chl,max}$) and the half saturation constant of phosphorus

965 ($K_{s,P}$). An increase (decrease) of $P_{chl,max}$ by one SD could increase (decrease) the European lake CH₄
 966 emissions by 0.77 Tg CH₄ yr⁻¹ or 79% (0.63 Tg CH₄ yr⁻¹ or 65%). This is again logical as a higher
 967 $P_{chl,max}$ indicates a stronger capacity of phytoplankton to assimilate carbon, thus resulting in higher
 968 amounts of organic carbon available for CH₄ production and emissions. The increase (decrease) of
 969 $K_{s,P}$ by one SD decreases (increases) the European lake CH₄ emissions by 0.46 Tg CH₄ yr⁻¹ or 48%
 970 (0.22 Tg CH₄ yr⁻¹ or 22%), a result which can be explained by a stronger TDP limitation of primary
 971 production when $K_{s,P}$ increases, resulting in lower CH₄ production and emissions. The next most
 972 sensitive parameters are the mineralization and burial rates (k_{20} and k_{bur}), for which an increase
 973 (decrease) in k_{20} by one SD result in an increase (decrease) of European lake CH₄ emissions by 0.19
 974 Tg CH₄ yr⁻¹ or 20% (0.39 Tg CH₄ yr⁻¹ or 40%), while an increase (decrease) of k_{bur} by one SD leads
 975 to a decrease (increase) of European lake CH₄ emissions by 0.35 Tg CH₄ yr⁻¹ or 36% (0.21 Tg CH₄
 976 yr⁻¹ or 22%). This is straightforward to interpret as a higher mineralization rate (k_{20}) will channel
 977 more mineralization into methanogenesis (and also via lower O₂ levels in the lake), while a higher
 978 burial rate (k_{bur}) translates to a lower relative amount of organic matter degradation, and thus lower
 979 CH₄ production and emissions.

980 The other parameters (including the shape parameter of the CH₄ production rate versus sediment
 981 depth α_{min} , the temperature dependence of mineralization θ , as well as the maximum CH₄ oxidation
 982 rate k_{max} and its temperature dependence $Q_{10,ox}$) are less sensitive, with their relative effects on
 983 European lake CH₄ emissions ranging from 1–20%. The shape parameter α_{min} can affect the CH₄
 984 emissions as it determines the split between diffusive and ebullitive pathways, i.e., a higher α_{min} favors
 985 a higher fraction of CH₄ emitted to water and atmosphere through the diffusive pathway, a pathway
 986 that is more prone to oxidation thus lowering total CH₄ emissions. We also find that a higher

987 temperature dependence of mineralization (θ) results in a lower CH₄ emission. This can be explained
 988 by the reference temperature of 20°C in the expression of the θ function, higher than the mean water
 989 temperature in most lakes, leading to a faster drop in mineralization for a larger θ when temperature
 990 is lower than 20°C. The parameter k_{max} barely impacts the total CH₄ emissions, as this parameter
 991 mostly influences the thickness of the water layers where the profiles of oxygen and methane overlap
 992 and the oxidation occurs, while the volume-integrated rates remain essentially unaltered (~~Regnier *et*~~
 993 ~~*al.*, 2011~~; Thullner and Regnier, 2019; Grossart *et al.*, 2011). As for the temperature dependence of
 994 oxidation ($Q_{10,ox}$), the sensitivity is even weaker because changing the $Q_{10,ox}$ value has a lower impact
 995 on the oxidation rates than changing k_{max} . Compared to other parameters (such as f_{mm} and $P_{chl,max}$),
 996 the relatively low effects of k_{max} and $Q_{10,ox}$ does not mean that the methane oxidation is not important,
 997 but highlight the dominant role of organic carbon production and decomposition on lake CH₄
 998 emissions, which were seldom simulated in previous models. Note that in our current model version,
 999 CH₄ oxidation only occurs through the aerobic pathway and thus neglects the potential additional
 1000 controls induced by anaerobic pathways (Mostovaya *et al.*, 2022; Su *et al.*, 2020).

1001 With the samples produced by the above sensitivity analysis and complemented by samples from
 1002 additional tests, we utilized a Random Forest (RF) model to assess the uncertainty of European lake
 1003 CH₄ emissions (see details in section 2.5.4). The RF model has a R^2 of 0.73 and Root of Mean Square
 1004 Error (RMSE) of 0.24 Tg CH₄ yr⁻¹ for the train set (Fig. 10a) and a R^2 of 0.52 and RMSE of 0.30 Tg
 1005 CH₄ yr⁻¹ for the out-of-bag samples (Fig. 10b), suggesting that ~~the~~ it can capture ~~well~~ the relationship
 1006 between model parameters and European lake CH₄ emissions well. Using these ensembles of CH₄
 1007 emissions, the uncertainty (or SD) of European lake CH₄ emissions associated with the choice of
 1008 biogeochemical parameter values was estimated as 0.23 Tg CH₄ yr⁻¹. Therefore, during the period of

1009 2010-2016, the European lakes (with surface areas between 0.1–1000 km²) have an annual mean
1010 emission of 0.97±0.23 Tg CH₄ yr⁻¹.

1011 With the RF model, we can also identify the importance of key model parameters involved as
1012 predictors (Fig. 10c). We noticed that the first four leading parameters are also the most sensitive
1013 parameters as identified in Table 43, while the importance of other parameters are slightly different
1014 from the sensitivity analysis. This slight difference can be attributed to the interactions of model
1015 parameters that are overlooked in the sensitivity analysis. Overall, from the sensitivity and uncertainty
1016 analysis, we find that the European lake CH₄ emissions are strongly controlled by the carbon
1017 biogeochemical dynamics, which, however, was not fully accounted for in previous lake models.

1018 **Table 43** Sensitivity of European lake CH₄ emissions (Tg CH₄ yr⁻¹) to key model
 1019 parameters. Mean and SD are the mean and standard deviation of a particular parameter.
 1020 Mean±SD indicates that the parameter values are adjusted by ± one SD; Mean±0.5SD
 1021 indicates that the parameter values are adjusted by ±0.5 SD.

Parameter setting		Mean±SD				Mean±0.5SD			
		-SD		+SD		-0.5SD		+0.5SD	
		<u>Absolute/percent</u>		<u>Absolute/percent</u>		<u>Absolute/percent</u>		<u>Absolute/percent</u>	
Primary production	P_{chl_max}	0.344	▲-65%	1.743	▲+80%	0.642	▲-34%	1.376	▲+42%
	$K_{c,P}$	1.432	▲+48%	0.754	▲-22%	1.170	▲+21%	0.852	▲-12%
Mineralization and burial rates	k_{20}	0.578	▲-40%	1.164	▲+20%	0.758	▲-22%	1.141	▲+18%
	k_{bur}	1.317	▲+36%	0.761	▲-22%	1.107	▲+14%	0.856	▲-12%
	θ	1.028	▲+6%	0.928	▲-4%	0.989	▲+2%	0.968	▲0%
	f_{mm}	0.302	▲-69%	1.888	▲+95%	0.605	▲-38%	1.437	▲48%
Methane oxidation	$K_{max}k_{mu}$	1.057	▲+9%	0.930	▲-4%	1.009	▲+4%	0.953	▲-2%
	α	0.992	▲+2%	0.983	▲+1%	0.978	▲+1%	0.973	▲0%
<u>Diffusion coefficient</u>	k_{diff}	1.124	▲+16%	1.046	▲+8%	1.068	▲+10%	1.048	▲+8%
Base value of the shape parameter	α_{min}	1.222	▲+26%	0.840	▲-13%	1.077	▲+11%	0.891	▲-8%

插入的单元格

插入的单元格

插入的单元格

插入的单元格

插入的单元格

插入的单元格

插入的单元格

插入的单元格

插入的单元格

插入的单元格

插入的单元格

插入的单元格

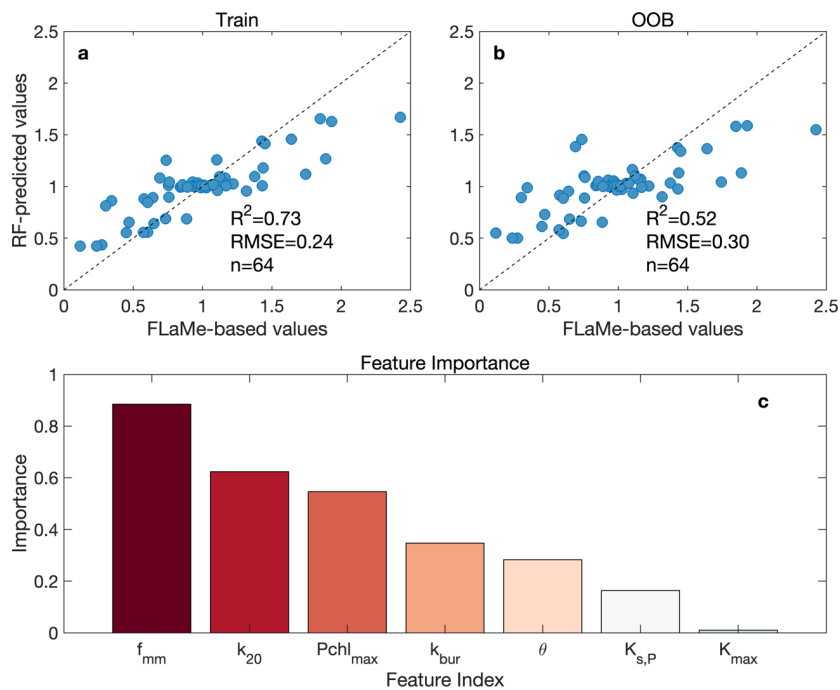


Fig. 10. Random Forest (RF) model for the uncertainty analysis. (a) and (b) are the train and test (Out-of-Bag prediction) of the RF model. (c) shows the importance of key model parameters. Note that the parameters of α_{min} and $Q_{10,ox}$ are excluded from illustration due to their second order of importance (indicated by negative values).

4. Model limitations

We have illustrated that FLaMe-v1.0 is able to capture complex physical-biogeochemical behaviors for lakes with diverse settings and environmental controls. Specifically, the FLaMe-model-v1.0 has been evaluated against (i) observational temporal variations of CH_4 fluxes at four contrasting, well-surveyed real lakes, (ii) the empirical ranges of primary production under different trophic status reported by Wetzel (2001), and (iii) observational patterns of CH_4 emissions against trophic and

1033 climate gradients spanning the European domain (Rinta *et al.*, 2017). Moreover, the European scale
1034 simulation produces a spatial pattern of lake CH₄ emission rates consistent with observation-based
1035 upscaling approaches (Johnson *et al.*, 2022). This continental scale application also demonstrates the
1036 power of our modelling framework that rests on a lake clustering approach and on a routing of nutrient
1037 (TDP) inputs from surrounding catchments to lakes that allow to account for eutrophication effects.
1038 Our results thus suggest that the FLame-v1.0 modelling framework performs well in providing
1039 reliable spatio-temporal patterns of lake CH₄ emissions at the ~~largeregional~~ scale: ~~(with lake areas~~
1040 ~~<1000 km²).~~ However, the results also pinpoint to several key aspects to be improved in the model
1041 and highlight critical data gaps that must be addressed in the future.

1042 First, the organic carbon module only accounts for autochthonous OC production as the substrate
1043 for methanogenesis, but ignores the contribution of allochthonous OC inputs leached from the
1044 ~~surrounding~~ catchments, rivers and streamflow. This is based on the distinct reactivity of
1045 autochthonous ~~andvs.~~ allochthonous OC inputs, with the latter being more refractory to ~~microbial~~
1046 ~~activities (mineralization and decomposition).~~ As a result, FLame-v1.0 may provide conservative
1047 estimates of CH₄ ~~productionsproduction~~ and ~~emissionsemission~~. However, neglecting the
1048 allochthonous C inputs may at the same time minimize the feedback of OC on light penetration,
1049 leading to systematically biased estimates ~~of autochthonous production~~ (section 2.2.2.1). Moreover,
1050 transient lake phosphorus dynamics and the co-limitations by nitrogen, albeit assumed to be less
1051 important, are neglected and might increase the uncertainty in the estimates of CH₄ production and
1052 emission. In addition, our primary production model does not resolve the short-term (e.g., (sub)daily)
1053 dynamics of algae growth induced by climate variability, rendering model-data comparison more
1054 difficult. In future model developments, these limitations could be addressed by (i) integrating or

1055 routing the lake water, carbon and nutrient fluxes along the global river network, which would allow
1056 to simultaneously solve the issue of time-invariant lake water levels in current global lake models
1057 (Golub *et al.*, 2022), including ours; (ii) refining the carbon module by incorporating more dynamic
1058 models for algal growth as well as P and N uptake and recycling processes within lakes.

1059 Second, several model assumptions and implementations are based on empirical or theoretical
1060 knowledge, which may lead to biases in the estimation of CH₄ fluxes. For instance, the present version
1061 of FLAME (i.e., v1.0) neglects the plant-mediated emission pathway (~~trough-rooted-plant~~) ~~in the~~
1062 ~~littoral-zone due to the lack of observational data for model calibration. Moreover through aerenchyma~~
1063 ~~in rooted plant) in the littoral zone (Mayr *et al.*, 2020; Zimmermann *et al.*, 2019) due to the lack of~~
1064 ~~observational data for model calibration. Moreover, a recently reported process, i.e., the horizontal,~~
1065 ~~advective littoral-pelagic transport of oxygen and methane (Doda *et al.*, 2024; Bouffard *et al.*, 2025)~~
1066 ~~was ignored for the following reasons: (1) The current FLAME-v1.0 relies on a 1-D vertical~~
1067 ~~representation while explicitly accounting for horizontal transport would require a 2-D framework;~~
1068 ~~and (2) observations related to horizontal transport remain limited, and whether this is an ubiquitous~~
1069 ~~feature of the CH₄ dynamics across a wide range of lakes will require further observational evidences.~~
1070 Furthermore, in our model, the lake is assumed to follow a “valley” shape. Although this is an
1071 advancement from the “bucket” shape used in previous process-based lake models of CH₄ emissions
1072 (e.g., LAKE 2.0, ABLM, and bLake4Me), it remains a simplified assumption that captures important
1073 but not all features of a realistic lake geometry. Furthermore, several benthic CH₄ processes are highly
1074 parameterized. For instance, the split between aerobic and anaerobic decomposition of organic matter
1075 is represented by a single parameter f_{mm} and is determined based on the data compilation from
1076 Bastviken (2022). This simplification leads to the same temperature dependence of CH₄ processes

1077 occurring in the sediment as that of pelagic and benthic mineralization. This is a shortcoming although
1078 it should be noted that the overall temperature dependence of CH₄ emissions, which results from the
1079 combined effects of OC production, mineralization, and subsequent CH₄ processes, was found to fall
1080 well within the observed ranges reported by Aben *et al.* (2017) (Fig. S21). The split of diffusive and
1081 ebullitive CH₄ fluxes is also currently captured by an empirically determined threshold depth ($z_{eb,min}$)
1082 based on limited observations by Langenegger *et al.* (2019). Moreover, the effects of heat transfer
1083 and CH₄ bubbles migration in the sediment are not resolved, which may lead to biased simulation of
1084 CH₄ fluxes especially for the timing. These are simplified representations related to the highly
1085 complex pathways of CH₄ production and emission, which needs to be improved by more mechanistic
1086 representations of the biogeochemical processes controlling carbon cycling, CH₄ production and
1087 transport via diffusion and bubble ascent. In addition, we acknowledge that the fixed grid spacing
1088 currently limits the model application to very shallow lakes, which could be solved by adopting a
1089 variable grid spacing scaling to the maximum lake depth.

1090 Third, different modules of the FLaMe-~~model-v1.0~~ could benefit from more comprehensive
1091 calibration and evaluation but those are limited by data availability. Although FLaMe-v1.0 has been
1092 evaluated against several timeseries of observed data collected in four well-surveyed lakes with
1093 contrasted dynamics, a full evaluation in the context of large-scale application would benefit from a
1094 significantly larger and representative set of observational data. Moreover, the *in-situ* climate
1095 conditions may vary greatly from the grid-level forcings, and the lake water dynamics may also affect
1096 the CH₄ fluxes significantly (e.g., Upper Mystic Lake; Varadharajan, 2009). Thus, a full
1097 comprehensive set of *in-situ* measurements of climate, water level, physical and biogeochemical
1098 variables would be highly valuable for the purpose of further model development, calibration and

1099 evaluation. At the European scale, we partly circumvented these limitations by evaluating lake
1100 primary production against the broad ranges reported by Wetzel (2001), and the simulated diffusive
1101 and ebullitive CH₄ fluxes across the environmental (nutrient and climate) gradients compiled by Rinta
1102 *et al.* (2017). In this context, complementary time-series of vertically resolved organic carbon, CH₄
1103 and O₂ concentrations, as well as high frequency measurements of CH₄ fluxes capturing short-lived
1104 emissions via the storage and ebullitive pathways and covering heterogeneity of CH₄ fluxes in large
1105 lakes (Denfeld *et al.*, 2018; Mayr *et al.*, 2020; Zimmermann *et al.*, 2019) would help further calibrate
1106 and evaluate the FLame-[model-v1.0](#). These measurements should be performed using a sufficiently
1107 large set of representative lakes covering the full range of lake morphologies, landscape properties,
1108 and climate.

1109 5. Conclusion and outlook

1110 In this study, we developed and tested a new process-based biogeochemical modeling framework
1111 (FLame-[v1.0](#)) to simulate lake CH₄ fluxes on the large-scale and, as a “proof of concept”, applied the
1112 model to European lakes. The physical lake model builds on the Canadian Small Lake Model (CSLM)
1113 and is coupled to a set of novel biogeochemical modules describing lake organic matter, oxygen and
1114 methane dynamics. We then showcased the abilities and performance of FLame-[v1.0](#) by: (1)
1115 analyzing the overall behaviors of the coupled C-O₂-CH₄ dynamics in two representative cases (a
1116 deep oligotrophic lake driven by cold climate in Northern Europe and a shallow eutrophic lake driven
1117 by warm climate in Southern Europe) as well as their decomposition, and (2) evaluating simulated
1118 temporal patterns of CH₄ fluxes against observations at four well-surveyed lakes with long-term
1119 timeseries. Simulation results were consistent with our common knowledge of lake CH₄ dynamics,
1120 suggesting that FLame-[v1.0](#) can capture the patterns of CH₄ production and emissions across

1121 different lake types as well as their responses to the changes in environment conditions, despite the
1122 complexity of underlying biogeochemical processes. Furthermore, by applying the model to boreal
1123 and central European lakes, we showed that FLaMe-[v1.0](#) captures well the observed magnitudes of
1124 both diffusive and ebullitive CH₄ fluxes as well as the difference between boreal and central lakes.
1125 Finally, at the European scale, FLaMe-[v1.0](#) estimates total CH₄ emissions from lakes ~~smaller than~~
1126 ~~with areas of 0.1–1000~~ km² (n=108407, total area = 1.33×10⁵ km²) as 0.97±0.23 Tg CH₄ yr⁻¹. In
1127 addition, the model resolves spatial patterns and seasonal variations of CH₄ emissions, providing a
1128 comprehensive view of their contribution to regional methane budgets.

1129 Despite some limitations in its current model configuration, this first version of FLaMe is a
1130 significant step forward in biogeochemical simulations of lake CH₄ dynamics. The model explicitly
1131 incorporates the dynamics of depth-integrated organic carbon cycling, such that the responses of
1132 organic carbon to climate and environmental change can be accounted for in estimating CH₄
1133 emissions. We also have incorporated the primary production as a function of total dissolved
1134 phosphorus loads from the surrounding catchments, allowing us to evaluate for the first time the
1135 impact of eutrophication on CH₄ emissions in a quantitative way. Moreover, our model is of
1136 intermediate complexity, and is thus designed for large scale applications. Although the model was
1137 run here at a coarse spatial resolution, its parallelized version offers the possibility to carry
1138 simulations at a finer resolution in the future. With these advancements, our model can be used to
1139 resolve the spatio-temporal variability of CH₄ emissions at regional and global scales under past and
1140 future climates, and has the potential to be coupled to Earth System Models to investigate the
1141 feedback between climate warming and global lake CH₄ emissions.

1142 **Data availability**

1143 The methane emission data for the four well-surveyed real lakes (Klöntal, Erssjön, Upper Mystic, and
1144 Villasjön) were obtained from Tan *et al.* (2024). The *in-situ* measurements of diffusive and ebullitive
1145 CH₄ emission rates in boreal and central European regions during late summer (August–September
1146 2010–2011) were obtained from Rinta *et al.* (2017). The lake characteristic information within Europe
1147 were obtained from the HydroLAKES database (Messenger *et al.* 2016):
1148 <https://www.hydrosheds.org/products/hydrolakes>. The meteorological variables from GSWP3-
1149 W5E5 reanalysis product were obtained from Inter-Sectoral Impact Model Intercomparison Project
1150 (ISIMIP3a): <https://www.isimip.org/gettingstarted/input-data-bias-adjustment/>.

1151

1152 **Code availability**

1153 The source codes for FLAME (Fluxes of Lake Methane) model version 1.0 are available at:
1154 <https://github.com/myFeng818/FLaMe-model-v1.0.git>. The preprocessing and postprocessing codes
1155 for the model can be obtained upon request.

1156

1157 **Acknowledgements**

1158 This study was supported by the Fonds National de la Recherche Scientifique of Belgium (F.R.S.–
1159 FRNS PDR T.0191.23), by the project of CLIMATE-SPACE RECCAP2: Global Land Carbon
1160 Budget and its Attribution to regional drivers, as well as by the project of ESM2025–Earth System
1161 Models for the Future (101003536). We acknowledge the climate modelling groups involved in
1162 ISIMIP3a for producing and making available their model outputs. Computational resources have

1163 been provided by the Consortium des Équipements de Calcul Intensif (CÉCI), funded by the Fonds
1164 de la Recherche Scientifique de Belgique (F.R.S.-FNRS) under Grant No. 2.5020.11 and by the
1165 Walloon Region.

1166

1167 **Author contributions**

1168 M.M., M.F. and P.R. designed the study, as well as the overall model strategy. M.M. and M.F. co-
1169 developed and tested the FLame model. D.B., S.A., R.L., A.J., G.G.L., M.D.M., and Z.T. provided
1170 plenty of valuable suggestions related to the model development. D.B. and S.A. also provided
1171 constructive suggestions on model evaluation against measurements and manuscript writing. M.D.M.
1172 helped us in setting up the CSLM at the beginning of developing FLame, Z.T. provided us the
1173 methane emission data from ISIMIP lake datasets, and W.T. helped us in collecting climate forcings
1174 from ISIMIP3a. M.M. and M.F. wrote the first version of the manuscript, and all coauthors helped in
1175 improving the manuscript.

1176

1177 **Competing interests**

1178 The authors declare no competing interests.

1179

1180 **Additional information**

1181 **Correspondence and requests for materials** should be addressed to M.F. (Maoyuan.feng@ulb.be)

1182

1183 **References**

- 1184 Aben, R.C.H., Barros, N., van Donk, E. *et al.*: Cross continental increase in methane ebullition under climate
1185 change. *Nat. Commun.*, 8, 1682. <https://doi.org/10.1038/s41467-017-01535-y>, 2017.
- 1186 Aristegui, J., Agustí, S. and Duarte, C. M.: Respiration in the dark ocean, *Geophys. Res. Lett.*, 30, 1041,
1187 <https://doi.org/10.1029/2002GL016227>, 2003.
- 1188 Bastviken D., Tranvik L. J., Downing, J. A., Crill, P. M., Enrich-Prast, A.: Freshwater methane emissions offset the
1189 continental carbon sink, *Science*, 331(6013), 50. <https://doi.org/10.1126/science.1196808>, 2011.
- 1190 Bastviken, D. (2022). Methane. In T. Mehner & K. Tockner (Eds.), *Encyclopedia of Inland Waters (Second Edition)*
1191 (pp. 136-154). Oxford: Elsevier.
- 1192 Bastviken, D., Cole, J., Pace, M., and Tranvik, L.: Methane emissions from lakes: Dependence of lake
1193 characteristics, two regional assessments, and a global estimate, *Global Biogeochem. Cycles*, 18, GB4009,
1194 <https://doi.org/10.1029/2004GB002238>, 2004.
- 1195 Behrenfeld, M. J. and Falkowski P. G.: Photosynthetic rates derived from satellite-based chlorophyll
1196 concentration, *Limnol. Oceanogr.*, 42, <https://doi.org/10.4319/lo.1997.42.1.0001>, 1997.
- 1197 [Bodmer, P., Bors, C., Liu, L. and Lorke, A.: Large sediment methane production potential in reservoirs compared](https://doi.org/10.1002/lno.70063)
1198 [to lakes and rivers. *Limnol. Oceanogr.*, <https://doi.org/10.1002/lno.70063>, 2025.](https://doi.org/10.1002/lno.70063)
- 1199 Boehrer, B. and Schultze, M.: Stratification of lakes, *Rev. Geophys.*, 46, 2006RG000210,
1200 <https://doi.org/10.1029/2006RG000210>, 2008.
- 1201 [Bouffard, D., Doda, T., Ramón, C. L., Ulloa, H. N.: Thermally driven cross-shore flows in stratified basins: a review](https://doi.org/10.1017/flo.2024.31)
1202 [on the thermal siphon dynamics. *Flow*. 2025;5:E1. doi:10.1017/flo.2024.31](https://doi.org/10.1017/flo.2024.31)
- 1203 Bouwman, A. F., Beusen, A. H. W., Billen G.: Human alteration of the global nitrogen and phosphorus soil
1204 balances for the period 1970–2050, *Global Biogeochem. Cycles*, 23, GB0A04,
1205 <https://doi.org/10.1029/2009GB003576>, 2009.
- 1206 Canadell, J. G., Monteiro, P. M. S., Costa, M. H., *et al.*: Global carbon and other biogeochemical cycles and
1207 feedbacks, Climate Change 2021: The Physical Science Basis: Working Group I Contribution to the Sixth
1208 Assessment Report of the Intergovernmental Panel on Climate Change, Cambridge University
1209 Press, Cambridge, United Kingdom and New York, NY, USA, 673-816, 2021.
- 1210 Carlson, C. A., Ducklow, H. W., Michaels, A. F.: Annual flux of dissolved organic carbon from the euphotic zone
1211 in the northwestern Sargasso Sea, *Nature*, 397, 405–408, 1994
- 1212 Cole, J. J., and Caraco, N. F.: Atmospheric exchange of carbon dioxide in a low-wind oligotrophic lake measured
1213 by the addition of SF₆, *Limnol. and Oceanogr.*, 4, <https://doi.org/10.4319/lo.1998.43.4.0647>, 1998.
- 1214 Deemer, B. R., Harrison, J. A., Li, S., *et al.*: Greenhouse Gas Emissions from Reservoir Water Surfaces: A New
1215 Global Synthesis. *Bioscience*, 66(11), 949-964. <https://doi.org/10.1093/biosci/biw117>, 2016.

Deemer, B. R., & Holgerson, M. A.: Drivers of methane flux differ between lakes and reservoirs, complicating global upscaling efforts. *J. Geophys. Res.-Biogeo.*, 126, e2019JG005600, <https://doi.org/10.1029/2019JG005600>, 2021.

DelSontro, T., Beaulieu, J.J., and Downing, J.A.: Greenhouse gas emissions from lakes and impoundments: Upscaling in the face of global change, *Limnol. Oceanogr. Lett.*, 3, 64-75, <https://doi.org/10.1002/lol2.10073>, 2018

Delwiche, K. and Hemond, H.F.: An enhanced bubble size sensor for long-term ebullition studies. *Limnol. Oceanogr. Methods*, 15, 821-835. <https://doi.org/10.1002/lom3.10201>, 2017

Denfeld, B. A., Baulch, H. M., del Giorgio, P. A., Hampton, S. E., and Karlsson, J.: A synthesis of carbon dioxide and methane dynamics during the ice-covered period of northern lakes, *Limnol. Oceanogr. Lett.*, 3, 117-131. <https://doi.org/10.1002/lol2.10079>, 2018.

Dlugokencky, E. J., Steele, L. P., Lang, P. M., Masarie, K. A.: The growth rate and distribution of atmospheric methane, *J. Geophys. Res.*, 99, 17021–17043, <https://doi.org/10.1029/94JD01245>, 1994.

Doda, T., Ramón, C. L., Ulloa, H. N., Brennwald, M. S., Kipfer, R., Perga M.-E., Wüest, A., Schubert, C. J., Bouffard, D.: Lake surface cooling drives littoral-pelagic exchange of dissolved gases. *Sci. Adv.* **10**, eadi0617(2024). DOI:10.1126/sciadv.adi0617

Frieler, K., *et al.*: Scenario setup and forcing data for impact model evaluation and impact attribution within the third round of the Inter-Sectoral Impact Model Intercomparison Project (ISIMIP3a), *Geosci. Model Dev.*, 17, 1–51, <https://doi.org/10.5194/gmd-17-1-2024>, 2024.

Forster, P. M., *et al.*: Indicators of Global Climate Change 2023: annual update of key indicators of the state of the climate system and human influence, *Earth Syst. Sci. Data*, 16, 2625–2658, <https://doi.org/10.5194/essd-16-2625-2024>, 2024.

Garnaud, C., MacKay, M., & Fortin, V.: A one-dimensional lake model in ECCO's land surface prediction system. *J. Adv. Model. Earth Syst.*, 14, e2021MS002861. <https://doi.org/10.1029/2021MS002861>, 2022.

Gatley, D. P., Herrmann, S., & Kretzschmar, H. J.: A twenty-first century molar mass for dry air, *HVAC&R Research*, 14(5), 655–662. <https://doi.org/10.1080/10789669.2008.10391032>, 2008.

Golub, M., *et al.*: A framework for ensemble modelling of climate change impacts on lakes worldwide: the ISIMIP Lake Sector, *Geosci. Model Dev.*, 15, 4597–4623, <https://doi.org/10.5194/gmd-15-4597-2022>, 2022.

Grasset, C., Mendonça, R., Villamor Saucedo, G., Bastviken, D., Roland, F. and Sobek, S.: Large but variable methane production in anoxic freshwater sediment upon addition of allochthonous and autochthonous organic matter. *Limnol. Oceanogr.*, 63: 1488-1501. <https://doi.org/10.1002/lno.10786>, 2018.

Grossart, H., Frindte, K., Dziallas, C., Eckert, W., Tang, K.W.: Microbial methane production in oxygenated water column of an oligotrophic lake, *Proc. Natl. Acad. Sci. U.S.A.* 108 (49) 19657-19661, <https://doi.org/10.1073/pnas.1110716108>, 2011.

Guillemette, F., von Wachenfeldt, E., Kothawala, D. N., Bastviken, D., Tranvik, L. J.: Preferential sequestration of terrestrial organic matter in boreal lake sediments, *J. Geophys. Res. Biogeosci.*, 122, 863–874, <https://doi.org/10.1002/2016JG003735>, 2017.

Hanson, P. C., Hamilton, D. P., Stanley, E. H., Preston, N., Langman, O. C., Kara, E. L.: Fate of Allochthonous Dissolved Organic Carbon in Lakes: A Quantitative Approach. *PLoS One*, 6(7): e21884, <https://doi.org/10.1371/journal.pone.0021884>, 2011.

Hanson, P. C., Buffam, I., Rusak, J. A., Stanley, E. H., Watras, C.: Quantifying lake allochthonous organic carbon budgets using a simple equilibrium model, *Limnol. Oceanogr.*, 59, <https://doi.org/10.4319/lo.2014.59.1.0167>, 2014

Harrison, J. A., Prairie, Y. T., Mercier-Blais, S., Soued, C.: Year-2020 global distribution and pathways of reservoir methane and carbon dioxide emissions according to the greenhouse gas from reservoirs (G-res) model, *Global Biogeochem. Cycles*, 35, e2020GB006888. <https://doi.org/10.1029/2020GB006888>, 2021.

Holgerson, M., and Raymond, P.: Large contribution to inland water CO₂ and CH₄ emissions from very small ponds. *Nature Geosci.*, 9, 222–226. <https://doi.org/10.1038/ngeo2654>, 2016.

Imberger, J.: The diurnal mixed layer, *Limnol. Oceanogr.*, 30, 737–770, <https://doi.org/10.4319/lo.1985.30.4.0737>, 1985.

Imboden, D.M., and Wüest, A.: Mixing Mechanisms in Lakes. In: Lerman, A., Imboden, D.M., Gat, J.R. (eds) *Physics and Chemistry of Lakes*. Springer, Berlin, Heidelberg. https://doi.org/10.1007/978-3-642-85132-2_4, 1995.

Lan, X., Thoning, K.W., and Dlugokencky, E.J.: Trends in globally-averaged CH₄, N₂O, and SF₆ determined from NOAA Global Monitoring Laboratory measurements. <https://doi.org/10.15138/P8XG-AA10>, 2024

Langenegger, T., Vachon, D., Donis, D., McGinnis, D.F.: What the bubble knows: Lake methane dynamics revealed by sediment gas bubble composition. *Limnol. Oceanogr.*, 64: 1526-1544. <https://doi.org/10.1002/lno.11133>, 2019.

Lauerwald, R., Regnier, P., Figueiredo, V., Enrich-Prast, A., Bastviken, D., Lehner, B.: Natural lakes are a minor global source of N₂O to the atmosphere. *Global Biogeochem. Cycles*, 33, 1564–1581. <https://doi.org/10.1029/2019GB006261>, 2019.

Lauerwald, R., Allen, G. H., Deemer, B. R., Liu, S., Maavara, T., Raymond, P., *et al.*: Inland water greenhouse gas budgets for RECCAP2: 2. Regionalization and homogenization of estimates. *Global Biogeochemical Cycles*, 37, e2022GB007658, <https://doi.org/10.1029/2022GB007658>, 2023.

1280 Lewis, W. M.: Global primary production of lakes: 19th Baldi Memorial Lecture, *Inland Waters*, 1(1), 1–28.
1281 https://doi.org/10.5268/IW-1.1.384_2011.

1282 Liikanen, A., Murtoniemi, T., Tanskanen, H., Väisänen, T., *Martikainen, P. J.*: Effects of temperature and oxygen
1283 availability on greenhouse gas and nutrient dynamics in sediment of a eutrophic mid-boreal
1284 lake, *Biogeochemistry*, 59, 269–286. https://doi.org/10.1023/A:1016015526712_2002

1285 Maavara, T., Lauerwald, R., Regnier, P., Van Cappellen, P.: Global perturbation of organic carbon cycling by river
1286 damming, *Nat. Commun.* **8**, 15347. https://doi.org/10.1038/ncomms15347_2017.

1287 Maavara, T., Lauerwald, R., Laruelle, G. G., Akbarzadeh, Z., Bouskill, N. J., Van Cappellen, P., Regnier,
1288 P. Nitrous oxide emissions from inland waters: Are IPCC estimates too high? *Glob Change Biol.*, 25, 473–
1289 448. https://doi.org/10.1111/gcb.14504_2019.

1290 MacIntyre, S., Bastviken, D., Arneborg, L., Crowe, A. T., Karlsson, J., Andersson, A., Gålfalk, M., Rutgersson, A.,
1291 Podgrajsek, E., Melack, J. M.: Turbulence in a small boreal lake: Consequences for air-water gas exchange,
1292 *Limnol. Oceanogr.*, 66(3):827–854. https://doi.org/10.1002/lno.11645_2020.

1293 MacKay, M. D., Versegny, D. L., Fortin, V., and Rennie, M. D.: Wintertime simulations of a boreal lake with the
1294 Canadian Small Lake Model, *J. Hydrometeorol.*, 18, 2143–2160, https://doi.org/10.1175/JHM-D-16-0268.1_2017.

1296 MacKay, M. D.: A process-oriented small lake scheme for coupled climate modeling applications, *J.*
1297 *Hydrometeorol.*, 13, 1911–1924, https://doi.org/10.1175/JHM-D-11-0116.1_2012.

1298 McGinnis, D. F., Greinert, J., Artemov, Y., Beaubien, S. E., Wüest, A.: Fate of rising methane bubbles in stratified
1299 waters: How much methane reaches the atmosphere? *J. Geophys. Res.*, 111, C09007,
1300 https://doi.org/10.1029/2005JC003183_2006

1301 Mendonça, R., Müller, R.A., Clow, D., Verpoorter, C., Raymond, P., Tranvik, L. J., Sobek, S.: Organic carbon
1302 burial in global lakes and reservoirs, *Nat. Commun.*, 8, 1694, https://doi.org/10.1038/s41467-017-01789-6_2017

1304 Messenger, M., Lehner, B., Grill, G., Nedeva, I., Schmitt, O.: Estimating the volume and age of water stored in global
1305 lakes using a geo-statistical approach. *Nat. Commun.*, 7, 13603, https://doi.org/10.1038/ncomms13603_2016.

1306 Martin, J. H., Knauer, G. A., Karl, D. M., Broenkow, W. W.: VERTEX: carbon cycling in the northeast Pacific,
1307 *Deep. Sea. Res. A.*, 34, 2, 267–285, [https://doi.org/10.1016/0198-0149\(87\)90086-0_1987](https://doi.org/10.1016/0198-0149(87)90086-0_1987).

1308 Mayorga, E., Seitzinger, S. P., Harrison, J. A., Dumont, E. Beusen, A. H. W., Bouwman, A. F., Fekete, B. M.,
1309 Kroeze, C., Van Drecht, G.: Global Nutrient Export from WaterSheds 2 (NEWS 2): Model development and
1310 implementation, *Environ. Model. Softw.*, 25, 7, 837–853, https://doi.org/10.1016/j.envsoft.2010.01.007_2010.

1311 Mayr, M. J., Zimmermann, M., Dey, J., *et al.*: Growth and rapid succession of methanotrophs effectively limit
1312 methane release during lake overturn. *Commun. Biol.*, 3, 108. https://doi.org/10.1038/s42003-020-0838-z_2020.

2020.

Mostovaya, A., Wind-Hansen, M., Rousteau, P., Bristow, L.A. and Thamdrup, B.: Sulfate- and iron-dependent anaerobic methane oxidation occurring side-by-side in freshwater lake sediment. *Limnol Oceanogr*, 67, 231–246. <https://doi.org/10.1002/lno.11988>, 2022

Jackson, R., Saunio, M., Bousquet, P., Canadell, J. G., Poulter, B., Stavert, A. R., Bergamaschi, P., Niwa, Y., Segers, A., Tsuruta, A.: Increasing anthropogenic methane emissions arise equally from agricultural and fossil fuel sources, *Environ. Res. Lett.*, 15, 071002, <https://doi.org/10.1088/1748-9326/ab9ed2>, 2020.

Johnson, M. S., Matthews, E., Du, J., Genovese, V., Bastviken, D.: Methane emission from global lakes: New spatiotemporal data and observation-driven modeling of methane dynamics indicates lower emissions, *J. Geophys. Res.-Biogeo.*, 127, e2022JG006793. <https://doi.org/10.1029/2022JG006793>, 2022.

Pajala, G., Sawakuchi, H. O., Rudberg, D., *et al.*: The effects of water column dissolved oxygen concentrations on lake methane emissions—Results from a whole-lake oxygenation experiment. *J. Geophys. Res.: Biogeo.*, 128(11), e2022JG007185. doi:10.1029/2022jg007185, 2023.

Petrescu, A. M. R., Qiu, C., Ciais, P., *et al.*: The consolidated European synthesis of CH₄ and N₂O emissions for the European Union and United Kingdom: 1990–2017, *Earth Syst. Sci. Data*, 13, 2307–2362, <https://doi.org/10.5194/essd-13-2307-2021>, 2021.

Petrescu, A. M. R., Qiu, C., McGrath, M. J., *et al.*: The consolidated European synthesis of CH₄ and N₂O emissions for the European Union and United Kingdom, 1990–2019, *Earth Syst. Sci. Data*, 15, 1197–1268, <https://doi.org/10.5194/essd-15-1197-2023>, 2023.

Rinta, P., Bastviken, D. Schilder, J., van Hardenbroek, M., Stötter, T., Heiri, O.: Higher Late Summer Methane Emission from Central Than Northern European Lakes, *J. Limnol.*, 76 (1), <https://doi.org/10.4081/jlimnol.2016.1475>, 2016, 2017.

Regnier, P., Dale, A.W., Arndt, S., LaRowe, D.E., Mogollón, J., Van Cappellen, P.: Quantitative analysis of anaerobic oxidation of methane (AOM) in marine sediments: A modeling perspective, *Earth-Sci. Rev.*, 106, 1–2, 105–130, <https://doi.org/10.1016/j.earscirev.2011.01.002>, 2011.

Reynolds, C. S.: The ecology of phytoplankton, Cambridge University Press, 2006

Rosentreter, J. A., Borges, A. V., Deemer, B. R., *et al.*: Half of global methane emissions come from highly variable aquatic ecosystem sources, *Nat. Geosci.*, 14(4), 225–230, <https://doi.org/10.1038/s41561-021-00715-2>, 2021.

Ruardij, P. & Van Raaphorst, W.: Benthic nutrient regeneration in the ERSEM ecosystem model of the North Sea, *Neth. J. Sea Res.*, 33, 3–4, 453–483, [https://doi.org/10.1016/0077-7579\(95\)90057-8](https://doi.org/10.1016/0077-7579(95)90057-8), 1995.

Saunio, M., Bousquet, P., Poulter, B., *et al.*: The global methane budget 2000–2012, *Earth Syst. Sci. Data*, 8, 697–751, <https://doi.org/10.5194/essd-8-697-2016>, 2016.

1346 Saunio, M., Stavert, A. R., Poulter, B., *et al.*: The Global Methane Budget 2000–2017, *Earth Syst. Sci. Data*, 12,
1347 1561–1623, <https://doi.org/10.5194/essd-12-1561-2020>, 2020.

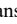
1348 Saunio, M., Martinez, A., Poulter, B., *et al.*, Global Methane Budget 2000–2020, *Earth Syst. Sci. Data Discuss.*,
1349 <https://doi.org/10.5194/essd-2024-115>, in review, 2024.

1350 Stavert, A. R., Saunio, M., Canadell, J. G., *et al.*: Regional trends and drivers of the global methane
1351 budget, *Glob. Change Biol.*, 28, 182–200. <https://doi.org/10.1111/gcb.15901>, 2021.

1352 Stepanenko, V., Mammarella, I., Ojala, A., Miettinen, H., Lykosov, V., and Vesala, T.: LAKE 2.0: a model for
1353 temperature, methane, carbon dioxide and oxygen dynamics in lakes, *Geosci. Model Dev.*, 9, 1977–2006,
1354 <https://doi.org/10.5194/gmd-9-1977-2016>, 2016.

1355 [Su, G., Zopfi, J., Yao, H., Steinle, L., Niemann, H. and Lehmann, M.F.: Manganese/iron-supported sulfate-](#)
1356 [dependent anaerobic oxidation of methane by archaea in lake sediments. *Limnol. Oceanogr.*, 65, 863-875.](#)
1357 <https://doi.org/10.1002/lno.11354>, 2020.

1358 Tan, Z., Zhuang, Q., and Anthony, K. W.: Modeling methane emissions from arctic lakes: Model development and
1359 site-level study, *J. Adv. Model. Earth Syst.*, 7, 459–483, <https://doi.org/10.1002/2014MS000344>, 2015.

1360 Tan, Z., Yao, H., Melack, J., Grossart, H.-P., Jansen, J., Balathandayuthabani, S., *et al.*  A lake biogeochemistry
1361 model for global methane emissions: Model development, site-level validation, and global applicability. *J. Adv.*
1362 *Model. Earth Syst.*, 16, e2024MS004275. <https://doi.org/10.1029/2024MS004275>, 2024.

1363 Thottathil, S. D., Reis, P. C. J., Prairie, Y. T.: Methane oxidation kinetics in northern freshwater
1364 lakes. *Biogeochemistry*, 143(1), 105–116. <https://www.jstor.org/stable/48701400>, 2019.

1365 Thullner, M., Regnier, P.: Microbial controls on the biogeochemical dynamics in the subsurface. *Rev. Mineral.*
1366 *Geochem.*, 85 (1): 265–302. <https://doi.org/10.2138/rmg.2019.85.9>, 2019.

1367 Van Drecht, G., Bouwman, A. F., Harrison, J., Knoop, J. M.: Global nitrogen and phosphate in urban wastewater
1368 for the period 1970 to 2050, *Global Biogeochem. Cycles*, 23, GB0A03,
1369 <https://doi.org/10.1029/2009GB003458>, 2009.

1370 Varadharajan, C.: Magnitude and spatio-temporal variability of methane emissions from a eutrophic freshwater lake,
1371 Thesis (Ph. D.)--Massachusetts Institute of Technology, Dept. of Civil and Environmental Engineering, 2009.

1372 Verseghy, D. L., and MacKay, M. D.: Offline Implementation and Evaluation of the Canadian Small Lake Model
1373 with the Canadian Land Surface Scheme over Western Canada. *J. Hydrometeor.*, 18, 1563–
1374 1582, <https://doi.org/10.1175/JHM-D-16-0272.1>, 2017.

1375 [Wanninkhof, R., Relationship between wind speed and gas exchange over the ocean revisited, *Limnol. Oceanogr.*](#)
1376 [Methods](#), 12, doi:10.4319/lom.2014.12.351, 2014.

1377 [Wanninkhof, R., Asher, W. E., Ho, D. T., Sweeney, C., McGillis, W. R.: Advances in quantifying air-sea gas](#)
1378 [exchange and environmental forcing, *Ann. Rev. Mar. Sci.*, 1, 213-44, https://doi.org/](#)

1379 10.1146/annurev.marine.010908.163742, 2009.

1380 Wetzel, R.G.: Limnology: Lake and River Ecosystems. Third Edition, Academic Press, San Diego, p389, 2001.

1381 William, R., Georgiy, K., Matti, L.: Basin-scale circulation and heat fluxes in ice-covered lakes, *Limnol.*
1382 *Oceanogr.*, 59, <https://doi.org/10.4319/lo.2014.59.2.0445>, 2014.

1383 Zhuang, Q., Guo, M., Melack, J.M., Lan, X., Tan, Z., Oh, Y., Leung, L. R.: Current and future global lake methane
1384 emissions: A process-based modeling analysis. *J. Geophys. Res.- Biogeo.*, 128,
1385 e2022JG007137, https://doi.org/10.1029/2022JG007137_2023.

1386 Zimmermann, M., Mayr, M. J., Bouffard, D., Eugster, W., Steinsberger, T., Wehrli, B., Brand, A. Bürgmann,
1387 H.: Lake overturn as a key driver for methane oxidation, preprint, <https://doi.org/10.1101/689182>, 2019.